INSTITUTO TECNOLÓGICO DE AERONÁUTICA

Rayssa Freitas Carvalho

A Posteriori Knowledge Based Digital Beamforming Concepts Demonstrated With Multi-Channel SAR-Data

Trabalho de Graduação
2016

Curso de Engenharia Eletrônica

CDU 621.396.67

Rayssa Freitas Carvalho

A Posteriori Knowledge Based Digital Beamforming Concepts Demonstrated With Multi-Channel SAR-Data

Orientadores

Dr. Sigurd Huber

Prof. Dr. Alexis Fabricio Tinoco Salazar

Divisão de Engenharia Eletrônica

SÃO JOSÉ DOS CAMPOS

INSTITUTO TECNOLÓGICO DE AERONÁUTICA

2016

Dados Internacionais de Catalogação-na-Publicação (CIP)
Divisão de Informação e Documentação

Carvalho, Rayssa Freitas
A Posteriori Knowledge Based Digital Beamforming Concepts Demonstrated With Multi-Channel SAR-Data / Rayssa Freitas Carvalho.
São José dos Campos, 2016.
Número de folhas no formato 68f.

Trabalho de Graduação – Divisão de Engenharia Eletrônica –
Instituto Tecnológico de Aeronáutica, 2015. Orientadores: Dr Sigurd Huber, Prof. Dr. Alexis Fabricio Tinoco Salazar

1. Radar de abertura sintética; 2.Largura da faixa; 3.Processamento de imagens; 4.Detecção de sinais; 5.Telecomunicações; 6.Engenharia eletrônica.

REFERÊNCIA BIBLIOGRÁFICA

CARVALHO, Rayssa Freitas; **A posteriori knowledge based digital beamforming concepts demonstrated with multi-channel SAR-Data**. 2016. 87f. Trabalho de Conclusão de Curso. (Graduação) – Instituto Tecnológico de Aeronáutica, São José dos Campos.

CESSÃO DE DIREITOS

NOME DO AUTOR: Rayssa Freitas Carvalho
TÍTULO DO TRABALHO: A Posteriori Knowledge Based Digital Beamforming Concepts Demonstrated With Multi-Channel SAR-Data
TIPO DO TRABALHO/ANO: Graduação /2016

Rayssa Freitas Carvalho
Rua H8A, 103 – Campus do CTA
12228-460 – São José dos Campos – SP

A POSTERIORI KNOWLEDGE BASED DIGITAL BEAMFORMING CONCEPTS DEMONSTRATED WITH MULTI-CHANNEL SAR-DATA

Essa publicação foi aceita como Relatório Final de Trabalho de Graduação

_____

Rayssa Freitas Carvalho
Autor

_____

Dr. Sigurd Huber (DLR-HR)
Orientador

_____

Prof. Dr. Alexis Fabrício Tinoco Salazar (ITA)
Orientador

_____

Prof. Dr. Cairo Lúcio Nascimento Júnior
Coordenador do Curso de Engenharia Eletrônica

São José dos Campos, 25 de Novembro de 2016.

Dedico este trabalho a todos os meus amigos

e a minha família

Acknowledgement

To have worked at DLR-HR was not only an amazing academic experience, but also an unique personal experience. From that I was able to write this thesis and also to enjoy the wonders of the European continent, especially Germany. For that opportunity, I thank Prof. Dr. Alberto Moreira, the responsible for the students exchange between ITA and DLR-HR.

I would like to thank the most Sigurd, my supervisor during my stay in DLR-HR, who helped me with all my doubts and supported me even when I was not in Germany anymore. Regarding professor Alexis, I thank him with all my heart for being not only my thesis supervisor, but also a life advisor, beyond academic issues.

I would also like to thank my parents, for always letting me go free to pursue my dreams and supporting me no matter what. To my teachers and professors, for being part of the journey that built who I am today.

At last but not least, a special thank you to my friends Lamounier, Matheus, Talles and Isabella, for being literally by my side while I wrote this work. I also thank Raffaela, Bernardo, Catarina, Thaís and all my Agita friends, for just being there when I needed the most. To my dear friend Artur, thanks for being my biggest partner during the university journey.

Resumo

Aplicações futuras de SAR, como monitoramento de desastres ou detecção de mudanças de biomassa em escala global exigem grandes larguras de faixas e alta resolução ao mesmo tempo. Uma alto resolução de azimute aumenta a necessidade de uma frequência de repetição de impulsos elevada (PRF) para amostrar o sinal adequadamente e evitar ambigüidades azimute no processo de imagem SAR. Contudo, o PRF elevado limita a largura da faixa. Para superar esta limitação, uma solução é dividir a antena receptora em múltiplas sub-aberturas e depois combinar os sinais das sub-aberturas usando *Beamforming* digital para suprimir as ambiguidades azimutais.

Uma vez que as técnicas de digitais de *Beamforming* digital requerem um conhecimento preciso dos diagramas de irradiação das antenas, uma primeira investigação desta tese trata da estimativa do diagrama complexo de irradiação de antenas a partir de dados de imagem dar de um alvo pontual. Estes diagramas estimados são então aplicados no processo de *beamforming*, o que significa que nenhuma informação a priori em termos de diagrama de irradiação é necessário. Aqui, basicamente, são apresentados dois conceitos, sendo o primeiro um otimizador de SNR eo segundo dedicado à supressão de ambigüidades de azimute.

Em uma segunda análise, a exigência de informação a priori é descartada quando a chamada matriz de covariância de ruído dos canais é estimada a partir dos dados.

Abstract

Future SAR applications such as disaster monitoring or detection of biomass changes on a global scale demand large swath widths and high resolution at the same time. A high azimuth resolution raises the need of a high pulse repetition frequency (PRF) in order to sample the signal adequately and avoid azimuth ambiguities in the SAR imaging process. However, the high PRF limits the swath width. To overcome this limitation, a solution is to split the receiving antenna into multiple sub-apertures and then combine the sub-apertures signals using digital beamforming techniques to suppress the azimuth ambiguities.

Since digital beamforming techniques require precise knowledge of the antenna patterns, a first investigation of this thesis deals with the estimation of the complex azimuth antenna patterns from point target data. These estimated patterns are then applied in an a posteriori beamforming process, meaning that no a priori information in terms of pattern knowledge is required. Here, basically two concepts are presented, the first being an SNR optimizer and the second dedicated to the suppression of azimuth ambiguities.

In a second analysis the requirement of no a priori information is dropped insofar that only the so called noise channel covariance matrix is estimated from the data. The beamforming is performed on the basis of the array steering vector, assumed to be known a priori.

Table of Contents

1 – Introduction

1.1 – Motivation and Objectives

Synthetic Aperture Radar (SAR) is a well proven imaging technique, finding application in various fields of natural sciences, military surveillance and security services.

However, conventional SAR systems are not capable of fulfilling the increasing demands for improved spatial resolutions and wide swath coverage, required for applications like Earth system dynamics monitoring [1], disasters management with shot revisit time and biomass changes monitoring on a global scale. The conventional SAR systems cannot meet these rising demands because unambiguous swath width and high azimuth resolution pose contradicting requirements on the system design [2].

To achieve a high azimuth resolution, a broad Doppler spectrum has to be acquired, what raises the need of a high Pulse Repetition Frequency (PRF) in order to sample the signal adequately and avoid azimuth ambiguities in the image. However, the high PRF limits the swath width. Alternative SAR imaging modes push this trade-off only further into one direction or another without resolving the constraint: the spotlight mode yields a high resolution but not sufficient coverage [3], while burst modes as ScanSAR [4,5] and TopSAR [6] map a wide swath but only with a coarse resolution.

One possibility to overcome this restriction is to transmit a signal using a broad beam, record the echo with multiple receivers and later combine the individual receiver signals using digital beamforming (DBF) techniques to reconstruct the high resolution image. In the classical approach a planar array antenna is employed [7,8], where the aperture is split on receive into several subapertures. Innovative DBF concepts and optimization strategies have been developed [9,10]. Although DBF techniques require the knowledge of the channels noise covariance matrix and the complex antenna patterns.

Adaptative beamforming has been approached in [11,12,13], but only in the sense of estimating the noise covariance matrix from the data, where the antenna patterns are assumed to be known a priori. Some other works has also been done showing different methods of estimating the noise covariance matrix [14,15,16,17].

Regarding the antenna patterns, methods of estimating the magnitude of the patterns from the data [18,19,20] have been derived, but no work was done so far to estimate the complex array manifold. This raises the need of the a priori knowledge of the complex patterns

to enable DBF techniques to be applied. Although, for spaceborne radars antenna pattern measurements are difficult to deploy from space and a priori measured or analytically calculated patterns are subjected to changes, what prohibits the efficient application of DBF techniques.

Motivated by that, the main objective of this thesis is to provide a posteriori knowledge based digital beamforming concept, where both the complex antenna patterns and the noise covariance matrix are estimated from multi-channel SAR data and later applied with DBF techniques to suppress azimuth ambiguities and optimize the image SNR.

1.2 – Structure of the Thesis

The thesis is structured in 7 chapters. Chapter 2 introduces the theoretical background, as the SAR principles and the planar array complex patterns formula. Chapter 3 presents the multi-channel SAR system principals, introducing DBF concept and two specific azimuth DBF techniques: Linear Constraint Minimum Variance (LCMV) beamforming and Minimum Variance Distortionless Response (MVDR) beamforming. Chapter 4 presents the method used to estimate the complex antenna patterns from SAR data employing a point target or transponder and also the method to estimate the noise covariance matrix from the data. Chapter 5 presents simulations where the estimated patterns are applied with DBF techniques to combine multiple channel signals in order to form a final high resolution image where azimuth ambiguities are suppressed or the SNR is optimized. Chapter 6 describes the experiment with a multi-channel demonstrator, with the aim of showing in practice the proposed method of pattern estimation.Chapter 7 presents the conclusions and suggestions for future work.

2 – Theoretical Background

2.1 – SAR Principles

SAR systems are active imaging systems operating at radio frequencies. This kind of radar is capable of obtaining an improved azimuth resolution compared to real aperture Radar (RAR) using signal processing and phase information of the successive recorded radar echoes. The radar radiates pulsed waveforms with duration τ_p at a pulse repetition frequency (PRF) and receives the backscattered echoes. As the pulse travels on the velocity of light, and this one is much higher than the velocity of the platform, the radar is considered stationary during the transmission of the pulses and reception of the corresponding echoes. After reception, the echoes are down-converted, sampled and stored in a matrix called the raw data matrix. After the raw-data processing, that is, range compression, range cell migration correction and azimuth compression, a focused two-dimensional image is obtained.

2.1.1 – SAR Acquisition Geometry

In Fig. 2.1 a simplified geometry of a side-looking radar is shown [2]. The radar is carried on a platform (aircraft or satellite) moving at speed V_s in a locally straight line at constant altitude. The radar beam is assumed to be directed perpendicular to the flight path of the vehicle and downwards to the Earth surface.

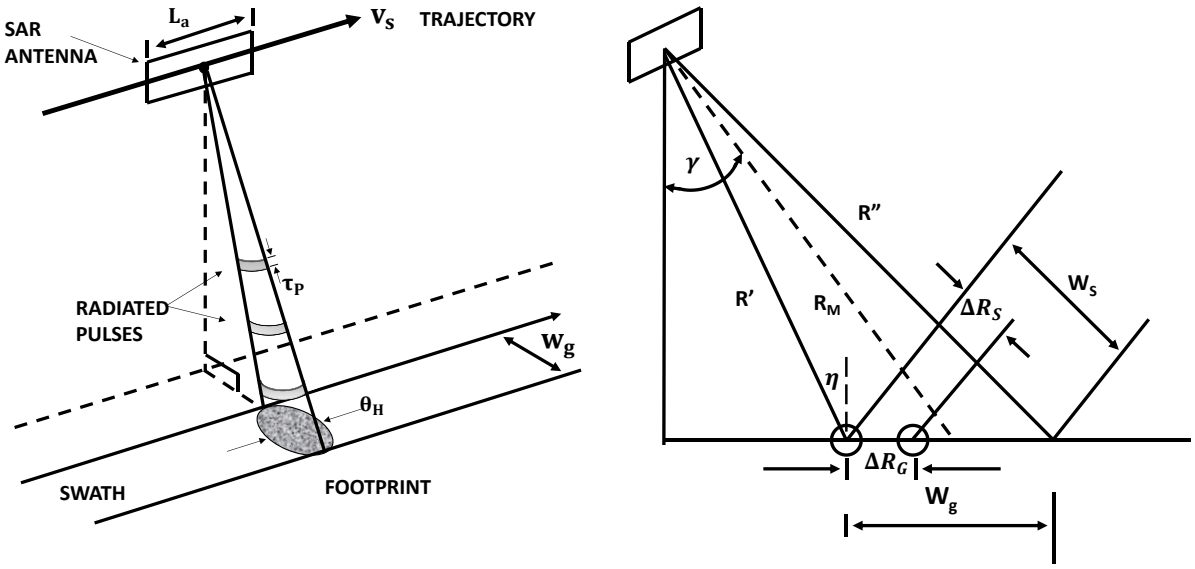

a) Perspective view

b) View in flight direction

Figure 2.1 –SAR acquisition geometry

For this geometry, the direction parallel to the radar movement is the *azimuth direction*, the direction parallel to line between the radar and the target is the *slant range direction* and its projection on the ground is called *ground range direction*. The area illuminated by the transmitting antenna is called footprint and its range extension is the ground swath width (W_g). The look angle γ, relative to the vertical, is the same as the incidence angle, η, which is the angle between the radar beam and the normal to the earth's surface at a particular point of interest.

2.1.2 – Range Resolution

The resolution of the radar in ground range (Fig. 2.1 b) is defined as the minimum range separation of two points that can be distinguished as separate by the system [1]. If the arrival time of the leading edge of the pulse echo from the more distant point is later than the arrival time of the trailing edge of the echo from the nearer point, each point can be distinguished in the time history of the radar echo. If the duration of the radar pulse is τ_p, the minimum separation of two resolvable points is then:

$$\Delta R_g = \frac{\Delta R_S}{\sin\eta} = \frac{c\tau_p}{2\sin\eta} \tag{2.1}$$

Where ΔR_S is the resolution in slant range and c is the speed of light.

To obtain a reasonable resolution ΔR_g, the required pulse duration τ_p would be too short to deliver adequate energy per pulse to produce a sufficient echo signal to noise ratio (SNR) for reliable detection. Therefore, a pulse compression technique is commonly used to achieve both high resolution (with a longer pulse) and high SNR. Processing the received pulse using matched filtering, the range resolution obtainable is:

$$\delta R_g = \frac{c}{2\,\mathrm{B_R}\sin\eta} \tag{2.2}$$

where B_R is the frequency bandwidth of the transmitted pulse.

All radar systems resolve targets in the range dimension in the same way. It is the resolution of targets in the azimuth dimension that distinguishes a SAR from other radar systems.

2.1.3 – Azimuth Resolution

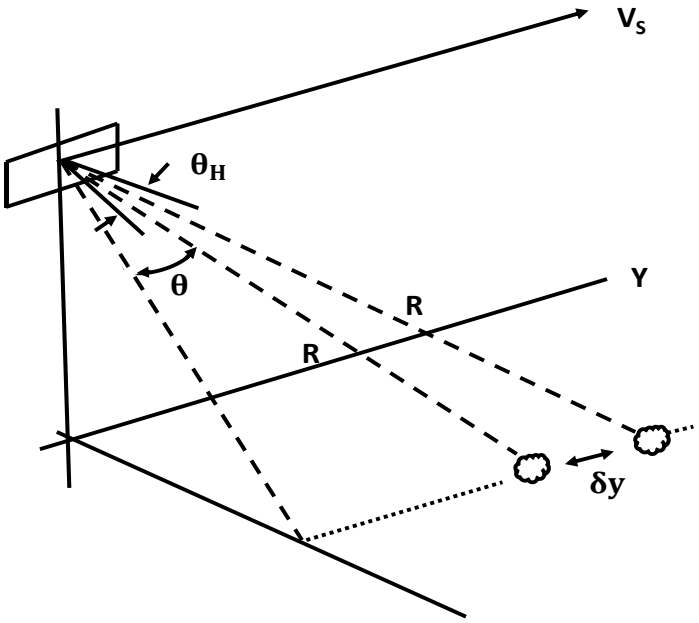

Figure 2.2 – Real Aperture Radar azimuth resolution

As shown in Fig. 2.1, L_a is the antenna length in the azimuth direction [2]. Then the antenna azimuth beamwidth θ_H is given by:

$$\theta_H \approx \frac{\lambda}{L_a} \tag{2.3}$$

where λ is the wavelength. For the conventional real aperture radars , two targets on the ground separated by δy in the azimuth direction and at the same slant range R (Fig. 2.2) can only be resolved if they are not in the radar beam at the same time, leading to an azimuth resolution of:

$$\delta y^{RAR} = R\theta_H \approx \frac{R\lambda}{L_a} \tag{2.4}$$

From equation (2.4), to improve the azimuth resolution δy^{RAR} for the RAR at a specific slant range R and wavelength λ, it is necessary to increase the antenna length in the azimuth dimension. For spaceborne imaging radars with range distance of hundreds of kilometers, to achieve a high resolution required for use in scientific application, it would be necessary an antenna of impractical length L_a and problematic to deploy in space.

The observation that led to SAR and improved the azimuth resolution was the one that two point targets, at slightly different angles with respect to the track of the radar, have different speeds at relative to the platform. Therefore, the radar pulses reflected from the targets will have different Doppler frequency shifts.

For a target at slant range R and azimuth coordinate y relative to the radar as shown in Fig. 2.2, the Doppler shift relative to the transmitted frequency is given by:

$$f_D = \frac{2V_s \sin\theta}{\lambda} = \frac{2V_s y}{\lambda R} \tag{2.5}$$

where V_s is the platforms velocity and θ is the angle of target relative to the platform as shown in Fig. 2.2. If the frequency of the signal is analyzed, any energy observed in a return time corresponding to range R and at Doppler frequency f_D will be from a target at azimuth coordinate:

$$y = \frac{\lambda R f_D}{2V_S} \tag{2.6}$$

So even though the targets are in the same range and in the beam at the same time, they can be discriminated by the analysis of the Doppler frequency. Now there are two coordinates to distinguish the targets. The echo time delay τ gives the range R and the Doppler frequency shift f_D gives the azimuth distance y relative to a point directly beneath the vehicle as shown in Fig. 2.2.

With the use of Doppler analysis of the echoes, the resolution δy in the azimuth coordinate is related to the resolution δf_D of the measurement of the Doppler frequency.
From equation (2.6), the azimuth resolution for the SAR is then:

$$\delta y^{SAR} = \frac{\lambda R \delta f_D}{2V_S} \tag{2.7}$$

The measurement resolution in the frequency domain is the inverse of the time interval T_{ia} of the waveform being analyzed, that is the time which a particular target remains in the beam. From Fig. 2.3 this time extension, called illumination time, is:

$$T_{ia} = \frac{R\theta_H}{V_S} \approx \frac{R\lambda}{L_a V_S} \tag{2.8}$$

which results in

$$\delta f_D = \frac{1}{T_{ia}} \approx \frac{L_a V_S}{R\lambda} \tag{2.9}$$

Substituting equation (2.9) into equation (2.7):

$$\delta y^{SAR} \approx \left(\frac{\lambda R}{2V_S}\right)\left(\frac{L_a V_s}{R\,\lambda}\right) = \frac{L_a}{2} \tag{2.10}$$

Equation (2.10) shows that the azimuth resolution for SAR depends only on the length of the antenna and it doesn't depend on the range distance R and wavelength λ.

2.1.4 – SAR Response to a Point Target

Since the theory of this thesis is based on SAR-Data for a strong point target, the system's response to a point target and the processing of this raw data will be further explored. The raw data is a two-dimensional matrix in which the range R and the azimuth position y are the coordinates. As the sensor moves in the azimuth direction, it transmits pulses in a frequency called pulse repetition frequency (PRF), the pulse is reflected by the target, the echo is received, quadrature-demodulated, digitized and put into the echo memory. As the velocity of light c is much higher than the velocity of the platform V_s, the azimuth position is considered constant during the time a pulse is transmitted and reflected back. Due to the movement of the platform, the time delay for echoes arriving from the point target is changing for each azimuth position and the variation of the time delay corresponds to the range variation and is called *Range Cell Migration.* The *Range Cell Migration* also causes an azimuth phase modulation, called *Azimuth Chirp*.

2.1.4.1 – Geometry and Parameter Definition

Fig. 2.3 shows a top view of the azimuth acquisition geometry considered here. For this geometry, the azimuth time zero is the moment of closest approach between the point target and the platform, t_{a1} is the azimuth time when the point target starts being illuminated, t_{a2} is the azimuth time when the point target stops being illuminated, R_0 is the slant range distance at the closest approach between the target and the platform, $R(t_a)$ is the slant range distance at

the considered azimuth time t_a, θ_H is the 3dB azimuth antenna beamwidth, V_S is the platforms velocity and $\theta(t_a)$ is the angle of the target off broadside at the considered azimuth time.

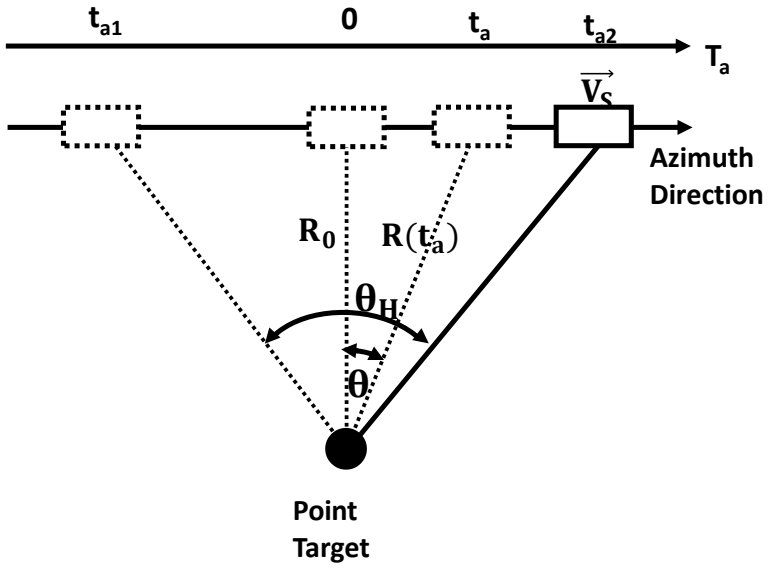

Figure 2.3 – Azimuth acquisition set up

From Fig. 2.3, the following equations can be inferred:

$$t_{a1} = -\frac{R_0}{V_S}\tan\left(\frac{\theta_H}{2}\right) \tag{2.11}$$

$$t_{a2} = \frac{R_0}{V_S}\tan\left(\frac{\theta_H}{2}\right) \tag{2.12}$$

$$R(t_a) = \sqrt{R_0^2 + V_S^2 t_a^2} \tag{2.13}$$

2.1.4.2 – Range Chirp Signal

The pulse most often used in SAR systems is the linear frequency modulated, or "chirp" pulse [21]:

$$s_r(t_r) = rect\left(\frac{t_r}{\tau_p}\right)\exp(j\pi k_r t_r^2) \tag{2.14}$$

Where τ_p transmitted pulse length in seconds, k_r is the range modulation rate in Hertz per second and t_r is the range time. From equation (2.14) we have that the phase variation of the range chirp over the range time $\Phi_{\mathrm{r}}(t_r)$ is given by:

$$\Phi_{\mathrm{r}}(t_r) = j\pi k_r t_r^2 \tag{2.15}$$

And from equation (2.15) we can obtain the range frequency variation $f_r(t_r)$:

$$f_r(t_r) = \frac{1}{2\pi} \cdot \frac{d\Phi_r}{dt_r} = k_r t_r \tag{2.16}$$

Equation (2.16) makes clear the linear frequency modulation characteristic of the chirp signal and also shows that the frequency excursion during τ_p generates the bandwidth of the transmitted signal $B_R = |k_r|\tau_p$.

The SAR images and SAR signal graphics of this section were simulated using the software IDL. The simulation parameters are listed in Table 2.1.

Table 2.1 – SAR data simulation parameters

Parameter	**Symbol**	**Value**
Range distance	R_o	500 m
Wavelength	λ	0,23 m
Antenna length in azimuth	L_a	0,35 m
Velocity of platform	V_S	75 m/s
Transmitted pulse duration	τ_P	10^{-5} m/s
Range modulation rate	k_r	-9.10^{12} s^{-2}
Transmitted pulse bandwidth	B_r	90 MHz
Speed of light	c	3.10^8 m/s
Pulse repetition frequency	PRF	600 Hz

Fig. 2.4 shows the simulated range chirp pulse, where Fig. 2.4 a) shows the range frequency, 2.4 b) shows the range phase,2.4 c) shows the imaginary part of the signal and 2.4 d) the real part of the signal.

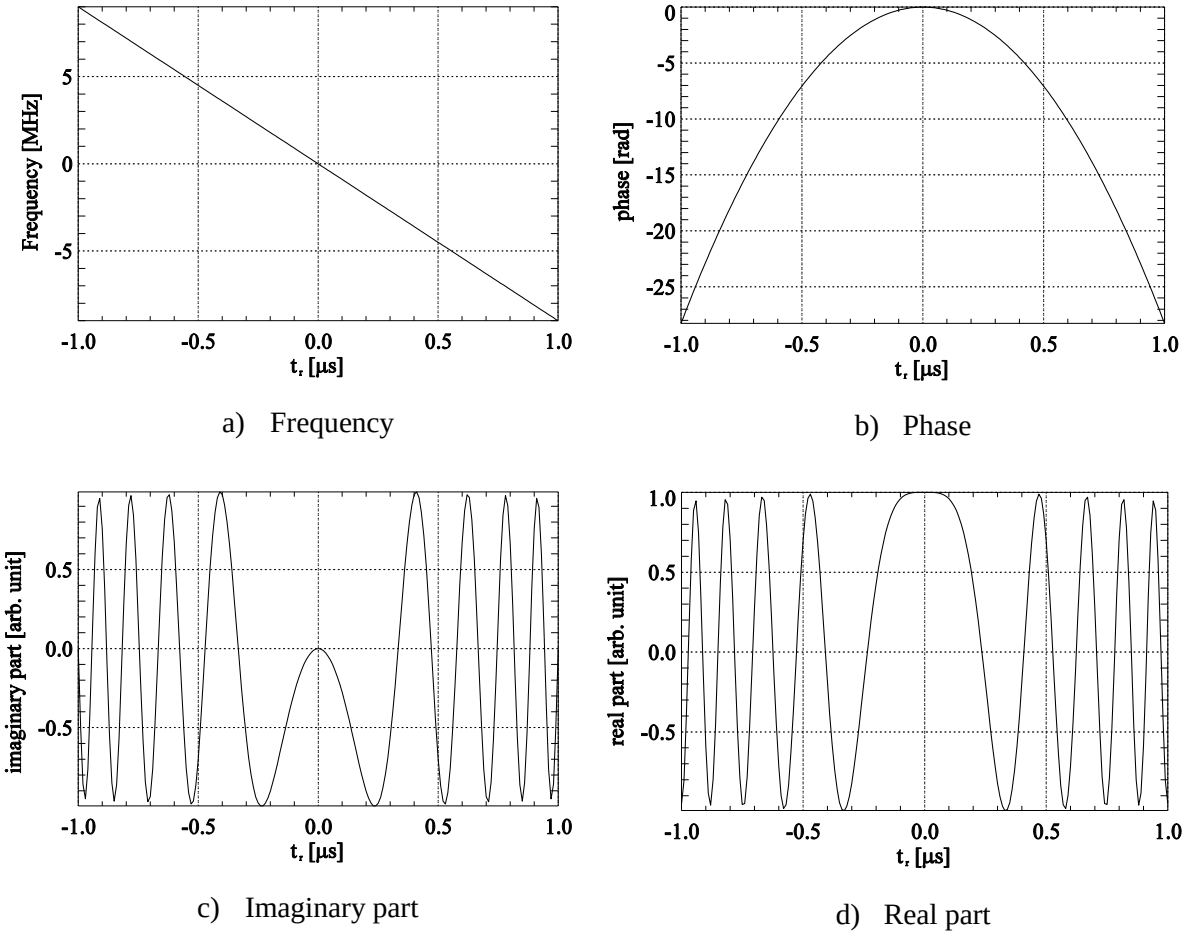

a) Frequency

b) Phase

c) Imaginary part

d) Real part

Figure 2.4 – Range Chirp pulse

2.1.4.3 – Azimuth Chirp Signal

Equation (2.13) shows that, as the platform moves along the azimuth direction, the slant range distance $R(t_a)$ to the target varies. This slant range variation is called range cell migration (RCM):

$$RCM = R(t_a) - R_0 = \sqrt{R_0^2 + V_S^2 t_a^2} - R_0 \tag{2.17}$$

Since the phase difference between transmitted and received waveforms due to two-way travel over the range $R(t_a)$ is [2]:

$$\Phi_a(t_a) = \frac{-4\pi R(t_a)}{\lambda} \tag{2.18}$$

This variation of the slant range distance causes an azimuth phase modulation, analog to the range chirp, called azimuth chirp. So the azimuth chirp signal is given by:

$$s_a(t_a) = \exp\left(j\frac{-4\pi R(t_a)}{\lambda}\right) \tag{2.19}$$

From equation (2.19) we can obtain the azimuth frequency $f_a(t_a)$:

$$f_a(t_a) = \frac{1}{2\pi}\cdot\frac{d\Phi_a}{dt_a} = \frac{-2V_S^2 t_a}{\lambda\sqrt{R_0^2 + V_S^2 t_a^2}} = \frac{-2V_S \sin[\theta(t_a)]}{\lambda} \tag{2.20}$$

And for a small processed azimuth beamwidth can be approximated to:

$$f_a(t_a) \approx \frac{-2V_S^2 t_a}{\lambda R_0} \tag{2.21}$$

Which is linear modulated.

Fig. 2.5 shows the simulated azimuth chirp signal, where Fig. 2.5 a) shows the azimuth frequency, 2.5 b) shows the azimuth phase, 2.5 c) shows the imaginary part of the signal and 2.5 d) the real part of the signal.

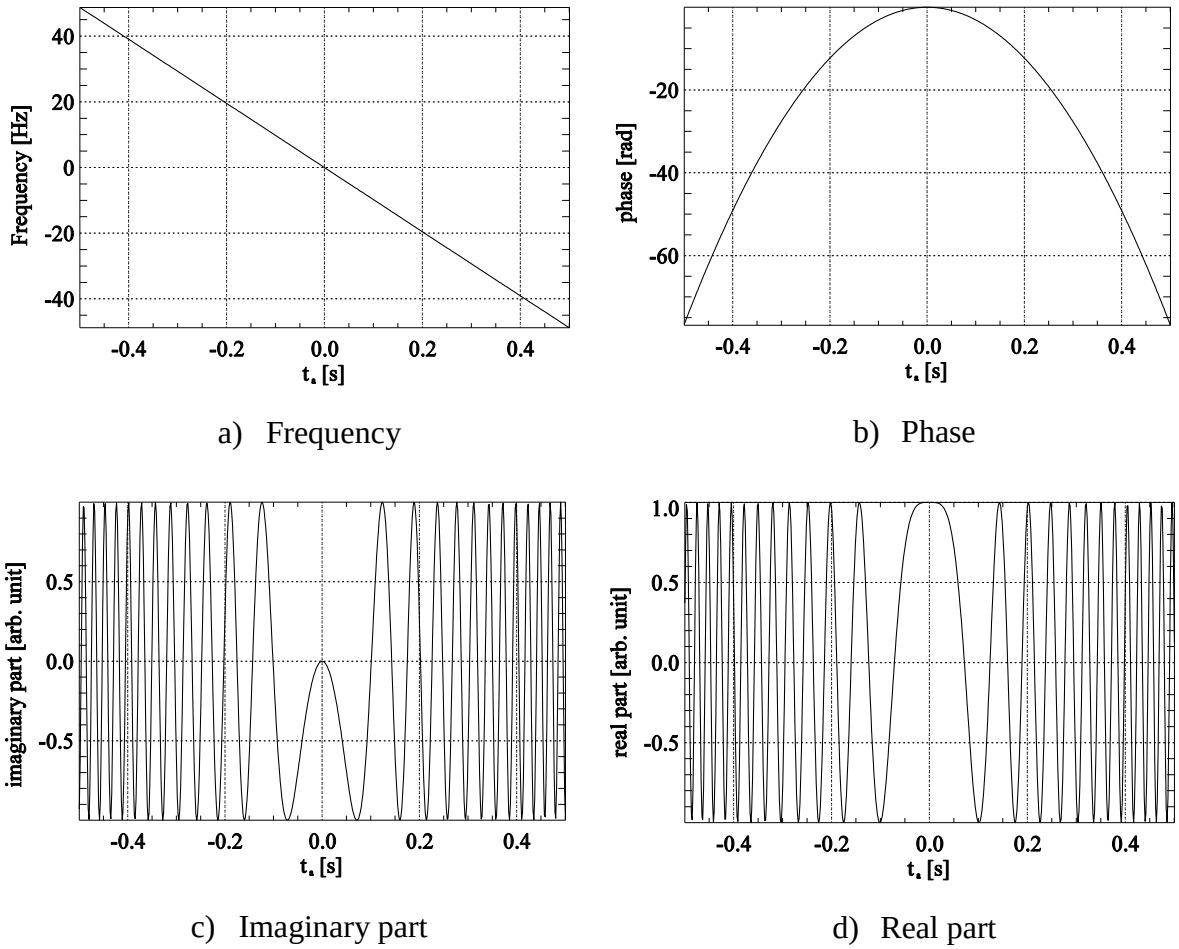

a) Frequency

b) Phase

c) Imaginary part

d) Real part

Figure 2.5 – Azimuth Chirp pulse

2.1.4.4 – SAR Raw Data of a point target

From sections 2.1.4.2 and 2.1.4.3, and also knowing that the time delay for the point target signal is:

$$\tau = \frac{2R(t_a)}{c} \tag{2.22}$$

The raw data signal of a point target is given by:

$$u(t_a, t_r) = \underbrace{a_{Tx}\big(\theta(t_a)\big)a_{Rx}\big(\theta(t_a)\big)}_{two-way\ pattern} s(t_a, t_r) + v(t_a) \tag{2.23}$$

$$s(t_a, t_r) = \\ = \sigma_0 \underbrace{rect\left(\frac{t_r - \frac{2R(t_a)}{c}}{\tau_p}\right) \exp\left(j\pi k_r \left(t_r - \frac{2R(t_a)}{c}\right)^2\right)}_{transmitted\ pulse} \cdot \underbrace{\frac{\exp\left(\frac{-4\pi R(t_a)}{\lambda}\right)}{(4\pi R)^2}}_{Green's function} \tag{2.24}$$

Where v is the thermal noise, a_{Tx} is the transmitting antenna pattern, a_{Rx} is the receiving antenna pattern, s is the received waveform, σ_0 is the backscattering coefficient, the factor $(4\pi R)^2$ is due to the attenuation on the propagation path between transmitter and target and due to the attenuation on the propagation path between target and receiver. Fig. 2.6 shows the simulated SAR raw data.

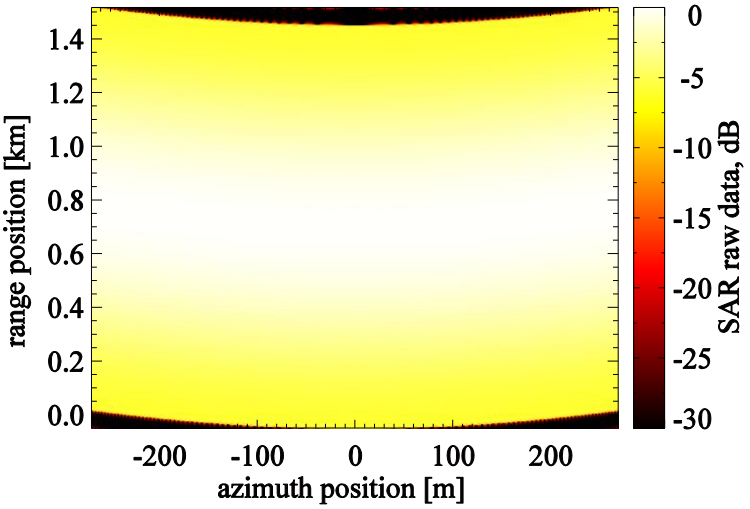

Figure 2.6 – SAR Raw data

2.1.5 – SAR Processing

To obtain a focused image, the raw data (Fig. 2.6) needs to be processed. In this section we will explore the processing of the raw data of a point target. The SAR Processor consists of three stages: range compression, range cell migration correction and azimuth compression.

2.1.5.1 – Range Compression

The range compression is performed in range frequency domain by a matched filter. Since the range chirp is given by equation (2.14), the corresponding matched filter in range time domain is:

$$H_r(t_r) = s_r^*(-t_r) = \exp[-j\pi k_r(-t_r)^2] \tag{2.25}$$

From equation (2.24) and equation (2.16), the range filter in the range frequency domain is:

$$H_r(f_r) = \exp\left(j\pi \frac{f_r^2}{k_r}\right) \tag{2.26}$$

So the range compression consists of four stages: fast Fourier transform (FFT) of each range line, calculation of range filter function, signal multiplication with range filter in frequency domain and finally the inverse fast Fourier transform (IFFT) in range.

Fig. 2.7 shows the simulated SAR data after range compression, where Fig. 2.7 a) shows the 2-D range compressed SAR data Fig. 2.7 b) shows one range- line of the range compressed data.

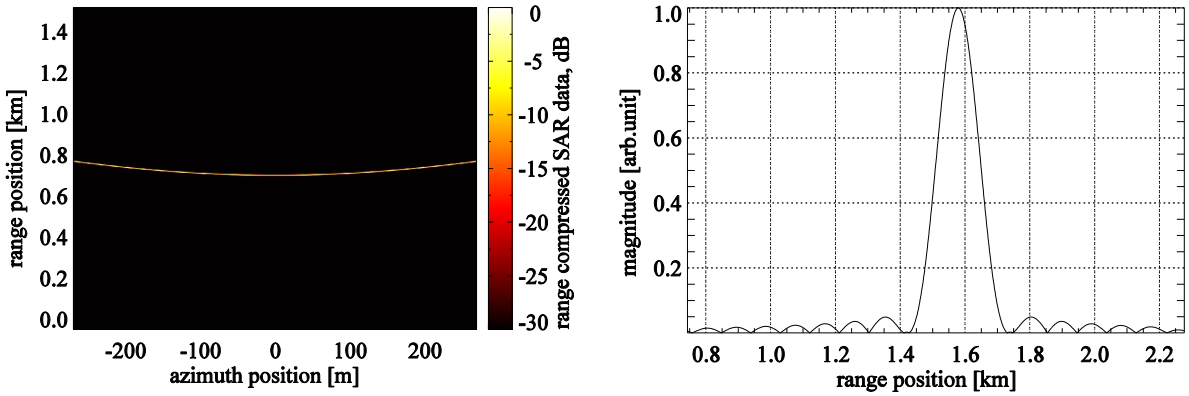

a) Range compressed SAR data

b) Range compressed raw data (one range line)

Figure 2.7 – Range compression

2.1.5.2 – Range Cell Migration Correction

As shown in equation (2.17), the range distance to the target varies with the position of the radar along its track and this variation is called range cell migration (RCM). Therefore, the numbers representing the system impulse response are found in data memory along a curved locus $R(t_a)$ [21]. A processing algorithm must acces the data and aligne it in a single range cell, corresponding to R_0, to later be compressed in azimuth along that trajectory. The processing algorithm is called range cell migration Ccrrection (RCMC).

From equation (2.22) the range time shift to perform RCM as function of the azimuth time is given by:

$$\Delta t_{RCMC}(t_a) = -(R(t_a) - R_0) \cdot \frac{2}{c} = -\left(\sqrt{R_0^2 + V_S^2 t_a^2} - R_0\right) \cdot \frac{2}{c} \tag{2.27}$$

From equation (2.27) and equation (2.20), the time shift as a function of the azimuth frequency is:

$$\Delta t_{RCMC}(f_a) = -\left(\frac{R_0}{\sqrt{1 - \left(\frac{\lambda f_a}{2V_S}\right)^2}} - R_0\right) \cdot \frac{2}{c} \tag{2.28}$$

From the property:

$$RCM_{phase} = -2\pi \cdot \Delta t_{RCMC}(f_a) \tag{2.29}$$

$$s(t_r - \Delta t_{RCMC}) = S(f_r)\exp(j \cdot RCM_{phase} \cdot f_r) \tag{2.30}$$

where $s(t_r)$ is the signal in the range time domain and $S(f_r)$is the signal in the range frequency domain. To perform RCMC the following stages have to be carried: FFT in azimuth, FFT in range, calculation of the phase for range time shift, multiplication of each range line with the linear phase function, IFFT in range and finally IFFT in azimuth.

Fig. 2.8 shows the simulated example of the SAR data after RCMC.

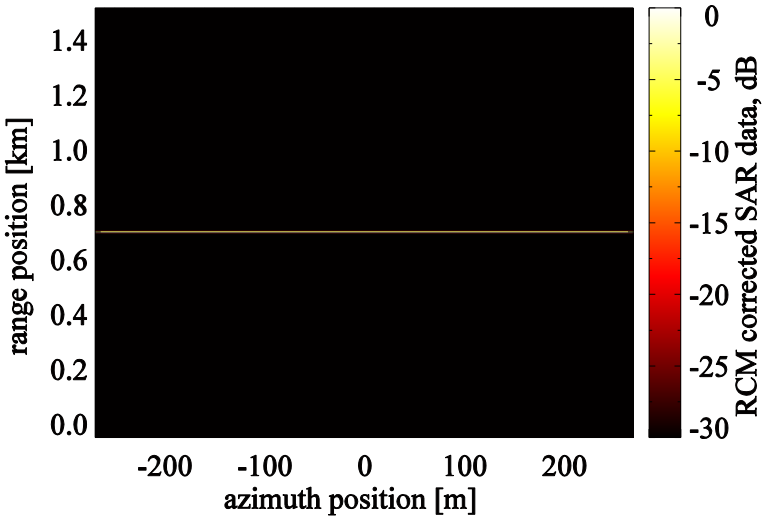

Figure 2.8– SAR data after range cell migration correction

2.1.5.3 – Azimuth Compression

The azimuth compression is performed in azimuth frequency domain by a matched filter. Since the azimuth chirp is given by equation (2.19), the corresponding matched filter in azimuth time domain is:

$$H_{az}(t_a) = \mathrm{s}_\mathrm{a}^*(-t_a) = \exp\left(j\frac{4\pi R(t_a)}{\lambda}\right) \tag{2.31}$$

From equation (2.31) and equation (2.20), the azimuth filter in azimuth frequency domain is given by:

$$H_{az}(f_a) = \exp\left[j\frac{4\pi}{\lambda}\cdot R_0\cdot\sqrt{1-\left(\frac{\lambda f_a}{2V_S}\right)^2}\right] \tag{2.32}$$

So the azimuth compression consists of four stages: FFT in azimuth, calculation of the azimuth compression filter for each range position, multiplication of each azimuth line with the filter function and IFFT in azimuth.

Fig. 2.10 shows the simulated example of the SAR data after azimuth compression.

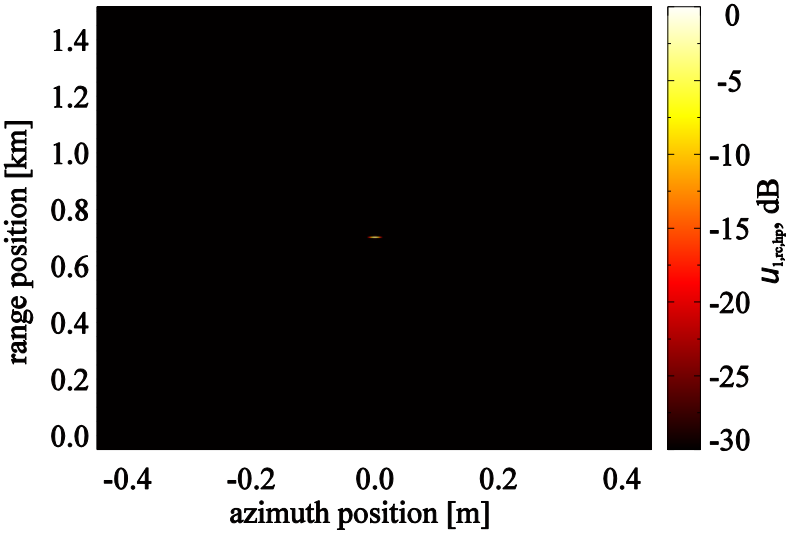

Figure 2.9 – SAR data after azimuth compression

2.1.6 – Limitation of Conventional SAR Systems

Conventional single-channel SAR systems are restricted with respect to their imaging capability. For these systems, wide swath coverage and high azimuth resolution pose contradicting requirements.

Due to the reception of the radar echoes at different azimuth positions, the SAR signal in azimuth is naturally discrete. So in order to avoid *azimuth ambiguities*, the frequency in which the echoes are acquired (PRF) must obey the *Nyquist-Shannon Sampling Theorem*:

$$PRF > B_D \tag{2.33}$$

Where B_D is the frequency bandwidth of the signal, that we can obtain from equation (2.20):

$$B_D = \frac{4V_S}{\lambda}\sin\left(\frac{\theta_H}{2}\right) \approx \frac{2V_s\theta_{\mathrm{H}}}{\lambda} = \frac{2V_S}{L_a} = \frac{V_s}{\delta y^{SAR}} \tag{2.34}$$

Combining Equation 2.33 and Equation 2.34, we have:

$$PRF > \frac{V_S}{\delta y^{SAR}} \tag{2.35}$$

Range ambiguities result from preceding and succeeding pulse echoes arriving at the antenna simultaneously with the desired return. In order to avoid the ambiguities required that the time of the reception of the earliest possible echo from any point in the swath due to a particular pulse transmission be later than the time of reception of the last possible echo from any other point due to transmission of previous pulse. If the near and far edges of the swath in the slant range are R' and $R"$ (Fig. 2.1 b), this requires that [2]:

$$\frac{2R''}{c} < \frac{2R'}{c} + T_p \tag{2.36}$$

Where $T_p = \frac{1}{PRF}$ is the time separation between two pulse transmissions. That implies that the swath width is bounded by:

$$W_S = R" - R' < \frac{c}{2PRF} \tag{2.37}$$

Equation (2.37) shows that high PRF limits the swath width. Combining equation (2.37) and equation (2.35) we have:

$$\frac{W_S}{\delta y^{SAR}} < \frac{c}{2V_S} \tag{2.38}$$

Equation (2.38) shows the classical SAR systems limitation of mapping broad swaths with simultaneously high azimuth resolution.

2.2 – Planar Array Antennas

Since this thesis is concerned with digital beamforming techniques, the topic of this section will be to introduce complex antenna pattern functions, which will be necessary for the formulation of digital beamforming theory.

The most used antenna type for SAR sensors are planar array antennas, and it is also the type of sensor used in the scope of this work.

As shown in Fig. 3.1, the elements are rectangular with dimensions a and b in x and y directions respectively. They are spaced with a distance d_x in the x-axis and d_y in the y-axis. The number of elements and antenna length on the x direction are respectively N_x and D_x, analogously N_y and D_y on the y direction.

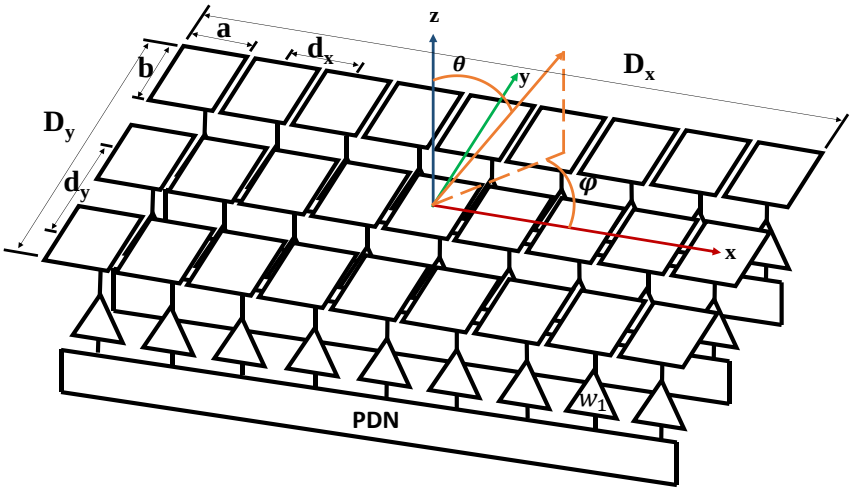

Figure 2.10 – Planar array antenna

The individual element patterns are [22]:

$$a_n(\theta,\varphi) = k\sqrt{\frac{ab}{\pi}}\,sinc\left(k\frac{a}{2}\sin\theta\cos\varphi\right)sinc\left(k\frac{b}{2}\sin\theta\sin\varphi\right)\times \\ \times\exp(jkdx_n\sin\theta\cos\varphi)\exp(jkdy_n\sin\theta\sin\varphi) \tag{2.39}$$

Where d_n is the x coordinate of the center of the element, and k the wavenumber, where:

$$k = \frac{2\pi}{\lambda} \tag{2.40}$$

3 – Multi-Channel SAR Systems

As seen in section 2.1.6, to obtain high azimuth resolution a broad antenna beam is required (equation 2.34), what raises the need of a high PRF in order to sample the signal adequately and avoid azimuth ambiguities (equation 2.35), but the high PRF limits the swath width (equation 2.37). To overcome this limitation, a solution is to employ multiple channels, undersample the signal and use digital beamforming techniques to combine the multiple channels signals to suppress the azimuth ambiguities.

In this chapter we will see the digital beamforming (DBF) concept and also some digital beamforming techniques for azimuth ambiguities suppression and also for SNR optimization.

3.1 – Digital Beamforming Concept

As we saw, the high PRF limits the swath width (equation 2.37). One possibility to overcome this restriction is to transmit a signal using a single transmitting element with a broad beam and to record the received echoes with multiple receivers [23].

Each channel is associated with a different complex far field pattern a_i associated and the raw signal of each channel is individually amplified, down-converted and digitized. As seen in equation (2.23) and again shown in equation (3.1), each channel raw signal is given by:

$$u_i = a_i s + v \tag{3.1}$$

Then beamforming via digital electronics is applied to reconstruct the high resolution image by processing and combining the individual receiver signals by means of weights, resulting on the DBF raw signal:

$$u_{DBF} = \boldsymbol{w}^T \boldsymbol{u} \tag{3.2}$$

Where $\boldsymbol{w}$ is the vector of weights and $\boldsymbol{u}$ the vector consisting of the raw data signal of the individual channels, defined respectively by:

$$\boldsymbol{w} = \left[w_1\, w_2 \ldots w_{N_{ch}}\right]^T \tag{3.3}$$

$$\boldsymbol{u} = \left[u_1\, u_2 \ldots u_{N_{ch}}\right]^T \tag{3.4}$$

In this thesis, a planar array antenna is employed, where the aperture is split on receive into multiple sub apertures. Fig. 3.1 shows a schematic of a multi-channel receiver with planar array antennas.

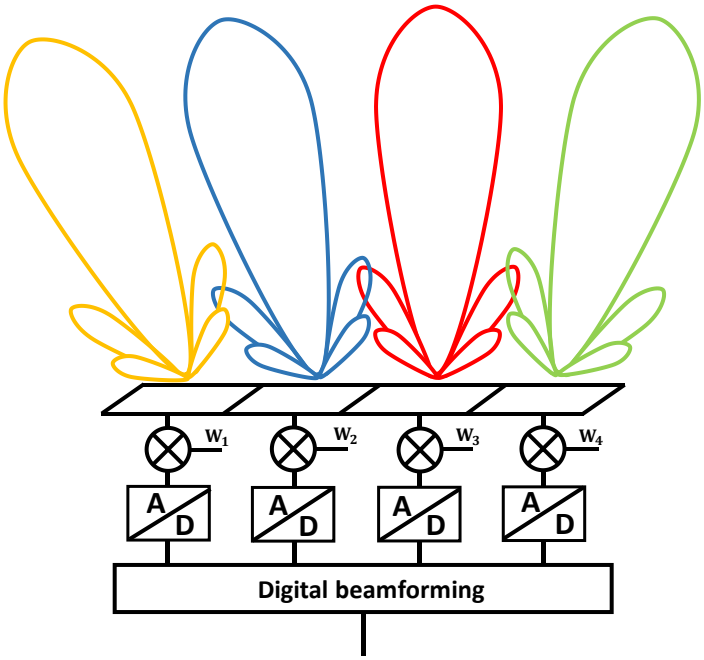

Figure 3.1 – Multi-channel receiver

3.2 – Digital Beamforming in Azimuth

To apply DBF in azimuth, a set of channels in this direction is used to reconstruct a single high gain signal subjected to certain constraints [23].

In this work, it is used as sensor an array of planar antennas, as depicted in Fig. 3.1, with the y-axis of the array aligned with the azimuth flight path, and as transmitting element it is used a single rectangular antenna.

Each channel is associated with a different complex pattern function $a_i(\theta, \varphi)$, where a_i here is the two-way pattern. The patterns a_i can be represented by the *array manifold*:

$$\boldsymbol{a}(\theta, \varphi) = \left[a_1(\theta, \varphi) \dots a_{N_{ch}}(\theta, \varphi)\right]^T \tag{3.5}$$

Where N_{ch} is the number of digital channels. Given that, the raw signals at each range time t_r and azimuth position y

$$\boldsymbol{u}(y, t_r) = \left[u_1(y, t_r) \dots u_{N_{ch}}(y, t_r)\right]^T \tag{3.6}$$

would be:

$$\boldsymbol{u}(y, t_r) = \boldsymbol{a}(\theta_D, \varphi_D)\boldsymbol{s}(y, t_r) + \boldsymbol{v} \tag{3.7}$$

where $\boldsymbol{v}$ represents the vector of white Gaussian noise and the direction (θ_D, φ_D), the direction of the source of the signal s. Since the topic is related to DBF in azimuth, it is considered the signals only over the spatial azimuth variable y, and the coordinate θ refers to the azimuthal plane ($\varphi = 90°$). So, according to equation (2.24) and neglecting the backscattering coefficient, since it is a constant and won't influence the DBF process, the received signal for a point target would be simply the green's function, independent of the range time:

$$s(y) = g(y) = \frac{\exp\left(\frac{-4\pi R(y)}{\lambda}\right)}{\left(4\pi R(y)\right)^2} \tag{3.8}$$

So the received signals analyzed are reduced to:

$$\boldsymbol{u}(y) = \boldsymbol{a}(\theta_D)s(y) + \boldsymbol{v} \tag{3.9}$$

Before applying the beamforming concepts, it is necessary to transform the signals into the azimuth wavenumber domain. The transformation is necessary because targets in different azimuth positions respond with different wavenumbers for a single azimuth position of the sensor, but signals of the two different targets are aligned with respect to the azimuth wavenumber when transformed to the frequency domain. So first, in order to form the high resolution image, each channel is reconstructed in the wavenumber domain on a grid with a high wavenumber sampling rate K_y'.

A way to relate space, represented by θ, and azimuth wavenumber k_y is:

$$k_y = -2k \sin\theta \tag{3.10}$$

Where k is the wavenumber as described by equation (2.40). The relation between the azimuth wavenumber k_y and Doppler frequency f_y , and between the azimuth sampling wavenumber K_y and PRF are:

$$k_y = 2\pi \frac{f_y}{V_S} \tag{3.11}$$

$$K_y = 2\pi \frac{PRF}{V_S} \tag{3.12}$$

Where V_S is the platform's velocity. Since the PRF or K_y limits the swath width, it has to be chosen as low as possible, and this lower bound is given by the diffraction limit of the array.

$$K_y \geq 4k \sin(\frac{\theta_{3dB_{array}}}{2}) \tag{3.13}$$

Where $\theta_{3dB_{array}}$ is the azimuth half-power beamwidth of the total receiver array.

The *i*th received raw-signal in the reconstructed grid with sampling rate K_y' is given by:

$$U_i(m\Delta k_y) = \frac{\Delta y}{V_S} \sum_{n=0}^{N-1} u_i(y(n\Delta y)) \exp[-jk_y(m\Delta k_y)y(n\Delta y)]$$
$$k_y \in \left[-\frac{K_y'}{2}, \frac{K_y'}{2}\right] \tag{3.14}$$

Where Δk_y is the wavenumber sampling increment:

$$\Delta k_y = \frac{2\pi}{Y} \tag{3.15}$$

Where Y is the complete analyzed azimuth path length. So we have that:

$$N = \frac{Y}{\Delta y} \tag{3.16}$$

$$M = \frac{Y}{\Delta y'} \tag{3.17}$$

$$\Delta k_y = \frac{K'_y}{\mathrm{M}} \tag{3.18}$$

where N is the number of samples of the undersampled channel signals and M is the number of samples of the reconstructed signal.

Since each channel is undersampled, ambiguous spectrums appear shifted by multiples of the sampling wavenumber K_y as shown in Fig. 3.2.

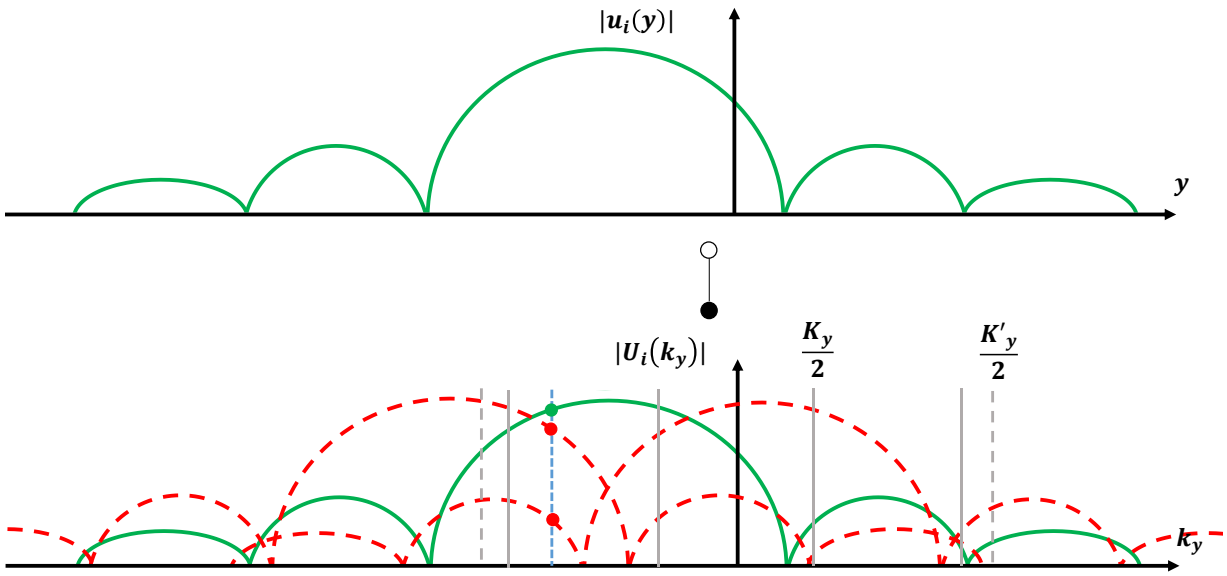

Figure 3.2 – Wavenumber domain representation of sampled signal

What is also shown in Figure 3.2 is the fact that the signals in wavenumber domain are modulated by the envelope of the azimuth antenna patterns.

It is enough to choose the sampling increment rate K'_y equal to the signal wavenumber bandwidth since no new information would be acquired by using a higher rate. So, from equations (2.34) and (3.12):

$$K'_y = 4k \sin\left(\frac{\theta_{3dB_{element}}}{2}\right) \tag{3.19}$$

Now, after the reconstruction, the individual channel spectra are combined for each wavenumber using DBF techniques by means of weights, choosing the weights to fulfill the application's necessity:

$$U_{DBF}(k_y) = \boldsymbol{w}^T(k_y)\boldsymbol{U}(k_y) \tag{3.20}$$

3.2.1 – LCMV Beamformer

From equation (3.20), to form the DBF signal, the individual channel signals are combined by means of weights and those weights are chosen according to the application's necessity. The principle of LCMV beamformer is to suppress the ambiguities while it minimizes the noise power. On this subsection, it will be shown how to obtain the weight vector that fulfill both constraints when applied on DBF.

We have that:

$$U_i(k_y) = \left[a_i\left(k_{y_D}\right)\cdots a_i\left(k_{y_{-1}}\right)\ a_i\left(k_{y_1}\right)\cdots\right]\left[S\left(k_{y_D}\right)\cdots S\left(k_{y_{-1}}\right)\ S\left(k_{y_1}\right)\cdots\right]^T + v_i \tag{3.21}$$

$$\boldsymbol{S}(k_y) = \left[S\left(k_{y_D}\right)\cdots S\left(k_{y_{-1}}\right)\ S\left(k_{y_1}\right)\cdots\right]^T \tag{3.22}$$

where the index D is associated to the signal of interest and the others are associated to the ambiguous signals. The angle θ is associated to the wavenumber k_y via equation (3.10). So we have that:

$$\boldsymbol{U}(k_y) = (\boldsymbol{AS} + \boldsymbol{v})(k_y) \tag{3.23}$$

where $\boldsymbol{A}$ is the array response matrix:

$$\boldsymbol{A} = \left[\boldsymbol{a}\left(k_{y_D}\right)\cdots\boldsymbol{a}\left(k_{y_{-1}}\right)\ \boldsymbol{a}\left(k_{y_1}\right)\cdots\right] \in \mathbb{C}^{N_{ch}\times N_{dir}} \tag{3.24}$$

where N_{dir} is the number of ambiguous directions to be suppressed. So from equations (3.20) and (3.23) the resulting DBF signal is:

$$\boldsymbol{U}_{DBF}(k_y) = (\boldsymbol{w}^T\boldsymbol{AS} + \boldsymbol{w}^T\boldsymbol{v})(k_y) \tag{3.25}$$

From equation (3.25), we have that to suppress ambiguities while keeping the signal of interest, the following constraint must be respected:

$$(\boldsymbol{A}^T\boldsymbol{w})(k_y) = \boldsymbol{c} \tag{3.26}$$

$$\boldsymbol{c} = [1\ 0 \cdots 0] \in \mathbb{C}^{N_{dir}\times 1} \tag{3.27}$$

When Equation 3.26 is applied to a certain k_y, locally it is created the beam:

$$\boldsymbol{w}^T\boldsymbol{a}(k_{y_D}) \tag{3.28}$$

That has a maximum at the analyzed wavenumber k_y and nulls on the corresponding ambiguous directions, that are shifted by multiples of the azimuth sampling wavenumber K_y.

The maximum number of directions that can be suppressed is limited by the number of channels, where N_{dir} maximum is $N_{ch} - 1$.

As the expected resulting power of the noise is given by:

$$P_v(k_y) = \boldsymbol{w}^T\boldsymbol{R_v}\boldsymbol{w}^* \tag{3.29}$$

where $\boldsymbol{R_v}$ is the noise covariance matrix:

$$\boldsymbol{R_v} = \mathcal{E}\{\boldsymbol{v}(k_y)\boldsymbol{v}^H(k_y)\} \tag{3.30}$$

where $\mathcal{E}\{\cdot\}$ denotes expectation value and $\{\cdot\}^H$ conjugate complex transpose. The weighting vector for LCMV beamformer is then obtained by minimizing equation (3.29) subjected to the constraint of equation (3.26). Its closed form solution is given by:

$$\boldsymbol{w}^*(k_y) = (\boldsymbol{R_v}^{-1}\boldsymbol{A}(\boldsymbol{A}^H\boldsymbol{R_v}^{-1}\boldsymbol{A})^{-1}\boldsymbol{c})(k_y) \tag{3.31}$$

3.2.2 – MVDR Beamformer

MVDR beamforming is not concerned with the suppression of ambiguities. Its objective is to minimize the noise power while it keeps the signal of interest.

From equation (3.25) we have that to keep the signal of interest the following constraint has to be respected:

$$\boldsymbol{a}^T\left(k_{y_D}\right)\boldsymbol{w} = 1 \tag{3.32}$$

So the weighting vector for MVDR beamformer is obtained by minimizing equation (3.29) subjected to the constraints of Equation (3.32). Its solution is given by:

$$\boldsymbol{w}^*(k_y) = \left(\frac{\boldsymbol{R_v^{-1}a}}{\boldsymbol{a}^H\boldsymbol{R_v^{-1}a}}\right)(k_y) \tag{3.33}$$

When equation (3.32) is applied to a certain k_y, locally is created the beam:

$$\boldsymbol{w}^T\boldsymbol{a}(k_{y_D}) \tag{3.34}$$

That has a maximum at the analyzed wavenumber k_y but no constraints are applied to the position of the nulls.

We can see from Equations 3.31 and 3.33 that to obtain the DBF weighting vector, it is required the knowledge of the array manifold and the noise covariance matrix.

4 – Estimation of Array Manifold and Noise Covariance Matrix

As seen previously on section 3.2 (equations 3.31 and 3.32), Digital Beamforming Techniques require precise knowledge of the array complex patterns and noise covariance matrix. But for spaceborne radars, antenna pattern measurements are difficult to deploy from space and a priori measured or analytically calculated patterns are subjected to changes due to calibration errors and other factors that may degrade the array. So an alternative of knowing a priori the antenna patterns is to estimate them from the data. Some previous work show methods of estimating the magnitude of antenna patterns from data [18,19,20], but no previous work was done so far to estimate the complex antenna pattern. In section 4.1, a method to estimate the array manifold from a point target SAR data, as well as the uncertainties that affects the methods performance, shall be discussed. So, the next step to drop the requirement of a priori information to apply DBF techniques, is to estimate the Noise Covariance Matrix from the data, which is approached on section 4.2.

4.1 – Complex Pattern Estimation Based on Strong Point Target

For this section, the simulated acquisition set up is the same as the one explained in subsection 2.1.4.1 and depicted in Fig. 2.3.

There is a sensor moving along the azimuth direction, that we called y, and there is a point target that was assumed to be fixed on the azimuth zero position. This target is on exactly cross distance of R_0 from the sensor. For each azimuth position of the sensor, there is an angle θ associated, that is the angle of the target off broadside, that is zero when the sensor and the target are exactly on the same azimuth position.

From equations (2.23) and (3.8) , for a strong point target (or a transponder) at y_0, the azimuth SAR signal for the i_{th} channel is given by:

$$u_i(y) = \sigma_o \cdot a_i(y, y_0) \cdot g_i(y, y_0) + v_i(y) \tag{4.1}$$

Where v_i is an additive noise, σ_o is the backscatteting coefficient of the target, a_i is the two-way antenna pattern of the channel and g_i is the Green's function, that is given by:

$$g_i(y, y_0) = \frac{\exp\left(\frac{-4\pi R(y, y_0)}{\lambda}\right)}{\left(4\pi R(y, y_0)\right)^2} \tag{4.2}$$

The simulation parameters are listed on Table 4.1.

Table 4.1 – Complex Patterns estimation simulation parameters

Parameter	**Symbol**	**Value**
Range distance	R_o	1,4 km
Wavelength	λ	0,24 m
Signal to Noise Ratio	SNR	10 dB
Number of array elements on the x direction	N_x	1
Number of array elements on the y direction	N_y	2
Array elements dimension on x direction	a	0,022 m
Array elements dimension on y direction	b	0,4 m
Spacing between array elements in the y-axis and	d_y	0,4 m
Antenna length on y direction	D_y	0,8 m
Speed of light	c	3.10^8 m/s

Fig. 4.1 shows the simulated example of the azimuth noisy signal of one of the channels, where Fig. 4.1 a) shows the magnitude of the signal and Fig. 4.1 b) shows the real part of the signal.

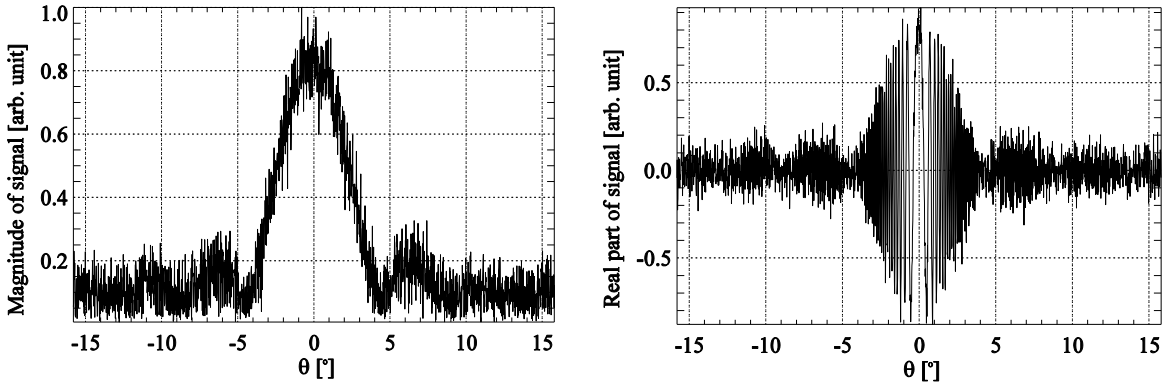

a) Magnitude of noisy signal

b) Real part of noisy signal

Figure 4.1 – Noisy signal

Now, given equation (4.1), a method consisting of three steps to estimate the complex antenna patterns is given bellow.

4.1.1 – First Step of Pattern Estimation

A first step to estimate the patterns would be to construct the Green's function from an estimate of the range history and then eliminate it from the signal. Ideally the range history is given by equation (2.13), so to construct the Green's function it is enough to apply equation (2.13) into equation (4.2).

Then an estimate of the complex antenna pattern can be derived eliminating the high frequency part of the signal, the Green's function, as:

$$\widehat{a_i}(y, y_0) = \frac{u_i(y)}{g_i(y,y_0)} = \frac{v_i(y)}{g_i(y,y_0)} + \sigma_o \cdot a_i(y, y_0) \tag{4.3}$$

Then we would have a noisy estimate of the pattern. The backscattering coefficient can be neglected because it is a constant and it is identical for all channels, so it doesn't affect the beamforming.

Fig. (4.2) shows the simulated example of the estimated noisy pattern for one channel, where Figure 4.2 a) shows the magnitude of the pattern and Figure 4.2 b) shows the real part of the pattern.

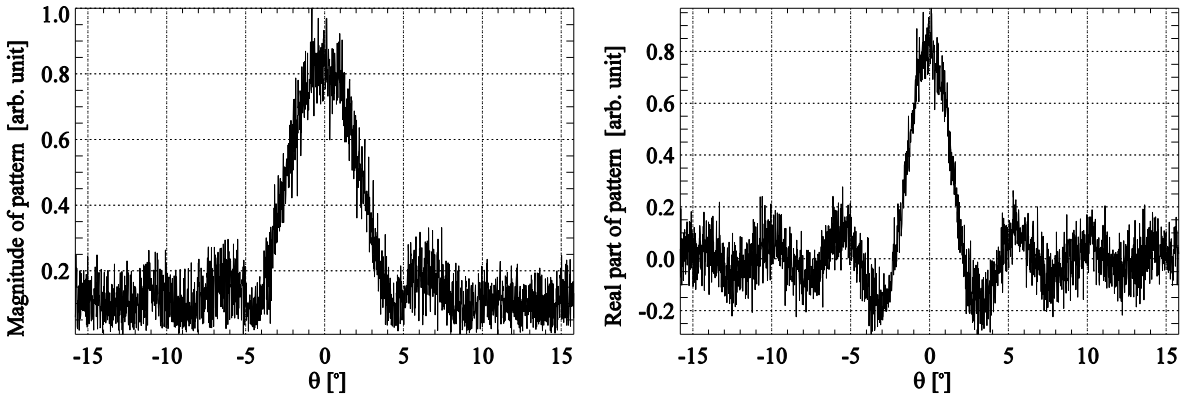

a) Magnitude of noisy pattern b) Real part of noisy pattern

Figure 4.2 –Noisy pattern

4.1.2 – Second Step of Pattern Estimation

Now that the Green's function was eliminated from the signal, which is the part of the signal broad in all the frequency domain, to eliminate the noisy and obtain a smooth pattern function estimate it may be done the Fourier Transform of the noisy estimated pattern and then apply a low pass filter to eliminate part of the noise. The bandwidth of the low pass is determined empirically, observing the spectrum of the pattern to determine which bandwidth would be appropriate.

Fig. 4.3 shows the simulated example of the Fourier transform of the noisy estimated pattern of one channel and Fig. 4.4 shows the Fourier Transform of the pattern after low pass filter.

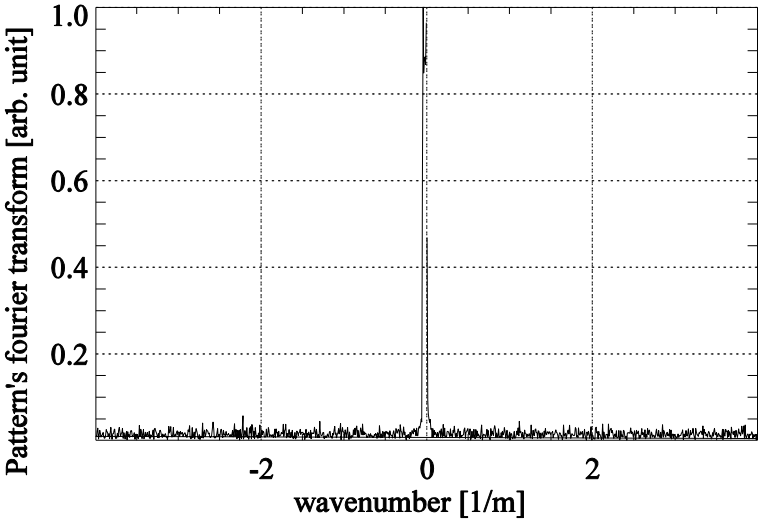

Figure 4.3 – Fourier transform of noisy pattern

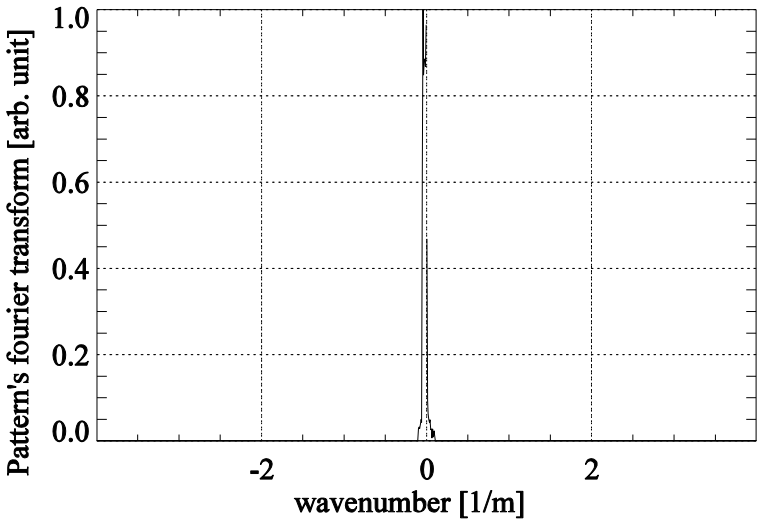

Figure 4.4 – Fourier transform of pattern after low pass filter

4.1.3 – Third Step of Pattern Estimation

The last step to obtain an estimate of the pattern is to do the inverse Fourier Transform of the low pass filtered spectrum.

Fig. 4.5 shows the simulated example of the comparison between the estimated and the analytical patterns for one channel, where the pattern in black is the estimated pattern and the pattern in red is the analytical pattern. Fig.4.5 a) shows the magnitude of the patterns and Fig. 4.5 b) shows the real part of the patterns.

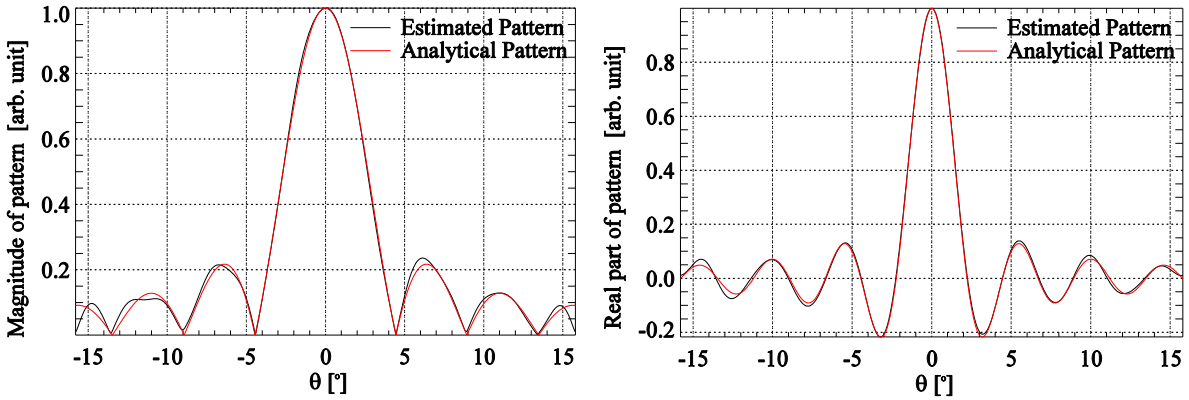

a) Magnitude of patterns b) Real part of patterns

Figure 4.5 – Comparison between Analytical and Estimated patterns

4.1.4 – Uncertainties in the Green's Function

The estimate of the Green's function plays the key role in the estimation of the complex pattern functions. It is constructed from an estimate of the objects range history. Therefore, the estimate of the Green's function takes the form:

$$\hat{g}_i(y, y_0) = \frac{\exp\left(\frac{-4\pi\hat{R}(y, y_0)}{\lambda}\right)}{\left(4\pi\hat{R}(y, y_0)\right)^2} \tag{4.4}$$

From a modelling approach, the estimate of the range history $\hat{R}(y, y_0)$ is interpreted as the true range history and an additive error $\Delta R(y, y_0)$:

$$\hat{R}(y, y_0) = R(y, y_0) + \Delta R(y, y_0) \tag{4.5}$$

Inserting equation (4.5) into equation (4.4) yields to:

$$\hat{g_i}(y, y_0) = \frac{\exp\left(\frac{-4\pi R(y, y_0)}{\lambda}\right)}{\left(4\pi R(y, y_0)\right)^2} \cdot \frac{\exp\left(\frac{-4\pi \Delta R(y, y_0)}{\lambda}\right)}{1 + \frac{2\Delta R(y, y_0)}{R(y, y_0)} + \frac{\Delta R(y, y_0)^2}{R(y, y_0)^2}} \tag{4.6}$$

Assuming that $R \gg \Delta R$, we have that:

$$\hat{g_i}(y, y_0) \approx g_i(y, y_0) \cdot \exp\left(\frac{-4\pi \Delta R(y, y_0)}{\lambda}\right) \tag{4.7}$$

From equation (4.7) we see that if the range error is considerably smaller compared to the range history, then the estimated Green's function is given by the correct Green's function multiplied by a phasor, that leads to a phase error on the estimated Green's function , that will be reflected on the phase of the estimated complex patterns (equation 4.3), but the magnitude of the estimated patterns may not be affected. If the error $\Delta R(y, y_0)$ is constant with azimuth, the phasor is a multiplying constant that will lead to just a constant shift of the estimated patterns' phase, that might not have influence on the DBF process. However, if $\Delta R(y, y_0)$ is azimuth dependent then the phase errors on the estimated pattern won't be constant and might influence the DBF process and suppression of ambiguities. The influence of errors on the Range history estimate, consequently on the Complex patterns estimate and on the DBF process will be analyzed in chapter 5.

4.1.5 – Noise Influence

Another factor that affects the estimation of the patterns is the noise. Fig. 4.5 shows simulated results of the effect of noise on the magnitude of the estimated patterns, where it presents the mean absolute error (Equation 4.8) according to the SNR of the signal used to estimate the complex pattern. The result is intuitive, that higher the SNR, lower the errors. The influence of the SNR on the DBF process and suppression of ambiguities will be further analyzed on chapter 5. The patterns mean absolute error is given by:

$$\delta(SNR) = \frac{\sum |\hat{a} - a|}{N_{samples}} \tag{4.8}$$

where â is the estimated pattern, a the analytical pattern and $N_{samples}$ the number of samples.

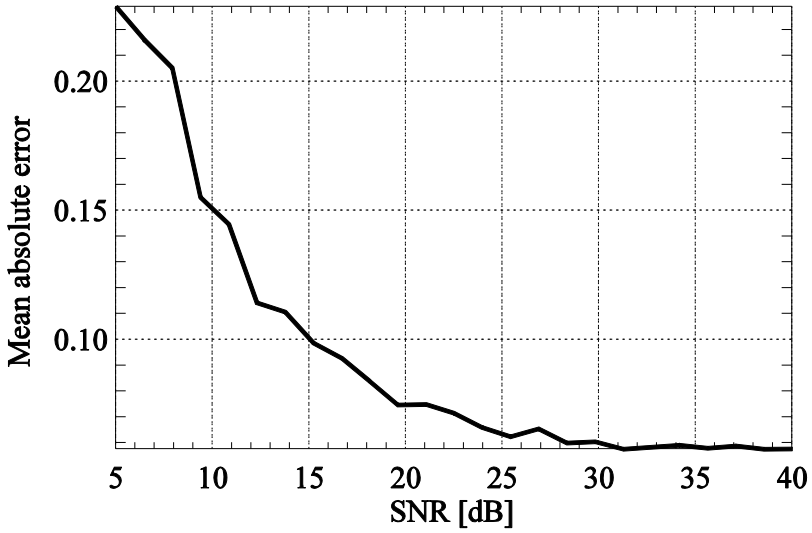

Figure 4.5 – Pattern estimation's sensitivity to noise

4.2 – Estimation of Noise Covariance Matrix

The next step to drop completely the requirement of a priori information to apply DBF techniques, is to estimate the Noise Covariance Matrix from the data, where it is given by:

$$\boldsymbol{R_v}(i,j) = \mathcal{E}\{\boldsymbol{v_i}\boldsymbol{v_j^*}\} \tag{4.9}$$

Where $\boldsymbol{v_i}$ is the noise for a given channel $\boldsymbol{i}$.

As the noise is a random variable and assuming that the noise of the individual channels are independent, $\boldsymbol{R_v}$ is ideally a diagonal matrix, where:

$$\boldsymbol{R_v}(i,j) = 0 \ , \ i \neq j \tag{4.10}$$

$$\boldsymbol{R_v}(i,j) = \sigma^2(\boldsymbol{v_i}) \tag{4.11}$$

A first way to estimate the Noise Covariance Matrix is to estimate it from noise-only measurements, when no signal is transmitted and only noise is measured. Then we have:

$$\boldsymbol{R_v}(i,j) = \mathcal{E}\{\boldsymbol{v_i}\boldsymbol{v_j^*}\} = \frac{\sum_N v_i v_j^*}{N_{samples}} \tag{4.12}$$

Or, for a signal with low SNR, which is typically the case for SAR signals, the noise covariance matrix can be approximated by the channel covariance matrix, so it can be estimated directly from the signal:

$$\boldsymbol{R_v}(i,j) \approx \boldsymbol{R_u}(i,j) = \mathcal{E}\{\boldsymbol{u_i u_j^*}\} = \frac{\sum_N u_i u_j^*}{N} \tag{4.13}$$

The estimation of noise covariance matrix and their application on the DBF process will be shown in chapter 5.

5 – Simulated Results of DBF Using Estimated Patterns and Noise Covariance Matrix

In this chapter simulated complex patterns and noise covariance matrices were estimated from SAR data applying the methods explained in chapter 4. Later, the estimated array manifolds and noise covariance matrices have been applied to the computation DBF weight vectors (equations 3.31 and 3.32), weight vectors that were used to combine multi-channel signals and obtain a final image with ambiguities suppressed or SNR optimized.

As explained previously in chapter 3, the signal is transmitted using a broad beam and then the echo is recorded with multiple receivers. As each channel is undersampled, azimuth ambiguities appear on positions with the corresponding Doppler frequency is equal to multiples of the PRF. So first the individual channel's signals are reconstructed in the wavenumber domain on a common grid with high sampling rate K_y'. Then the individual channels' spectra are combined by means of weights calculated by DBF techniques for each wavenumber using the estimated antenna patterns. At last, the resulting signal is retransformed to the time domain and azimuth compressed to obtain the focused image.

In this section all the simulated signals, the ones used to estimate the complex patterns and also the ones that were combined by DBF techniques to form the final signal, were simulated using the following parameters:

Table 4.1 – DBF simulation parameters

Parameter	Symbol	Value
Range distance	R_o	5 km
Wavelength	λ	0,031m
Pulse Repetition Frequency	PRF	125 Hz
Reconstruction wavenumber sampling rate	K_y'	$27{,}9\ m^{-1}$
Velocity of platform	V_S	90 m/s
Number of array elements on the x direction	N_x	1
Number of array elements on the y direction	N_y	9
Array elements dimension on x direction	a	1,8 m
Array elements dimension on y direction	b	0.2 m
Spacing between array elements in the y-axis and	d_y	0,4 m
Antenna length on y direction	D_y	1,8 m
Speed of light	c	3.10^8 m/s

According to Equations 2.33 and 2.34, the minimum PRF required to avoid azimuth ambiguities is 800.5 Hz, so indeed each channel is undersampled. According to equations (3.10) and (3.11), the minimum PRF so that the signal can be reconstructed on the DBF process is 92.6 Hz, so it was chosen 125Hz to have some margin.

As there are 9 channels, the maximum number of ambiguities that can be suppressed is 8. As the ambiguities appear on frequencies multiples of the PRF, from equations (3.10) and (3.11), considering the target at the azimuth position 0, the 8 first ambiguities appear at the azimuth positions of $\pm$108.5 m, $\pm$217.1 m, $\pm$326 m and $\pm$435.4 m.

The reconstruction sampling wavenumber K_y' was chosen according to equation (3.17), what gives us according to equation (2.34) an azimuth resolution of 22.5 cm.

5.1 – DBF- Range error free and Noiseless case

In this subsection all the simulated signals, the ones used to estimate the complex patterns and also the ones that were combined by DBF techniques to form the final signal, were simulated without noise so that some properties of DBF are made clear.

Fig. 5.1 a) shows the normalized compressed azimuth SAR signal of a point target reconstructed using MVDR beamforming. The red lines mark the first the first four left and right azimuth ambiguities. We can see that this DBF technique doesn't suppress the ambiguities. But when LCMV is applied (Fig. 6.1 b), we can see that the eight first ambiguities are suppressed.

On Fig. 5.2, a zoom of the LCMV signal of Fig. 5.1 b) is shown, so we can see that the resolution corresponds to the expected, around 22cm.

Fig. 5.3 a) shows the pattern after applying MVDR pointing at the zero Doppler frequency, obtained according to equation (3.32). Again we can see that no concern regarding the suppression of ambiguities is made. On Fig. 5.3 b) the pattern pointing at the zero Doppler frequency for the LCMV DBF is shown and we can see that there are nulls placed on the direction of the first eight ambiguities.

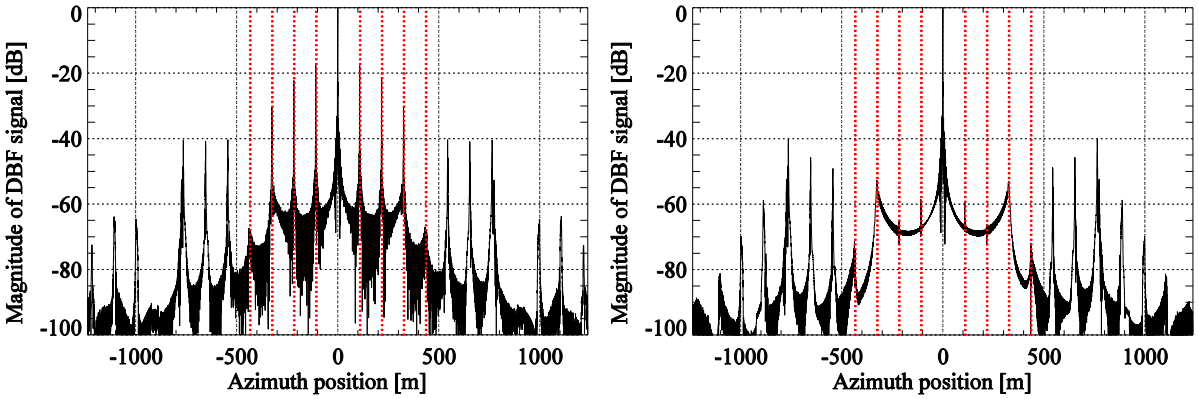

a) MVDR DBF b) LCMV DBF

Figure 5.1 – Magnitude of focused point target signal reconstructed using DBF

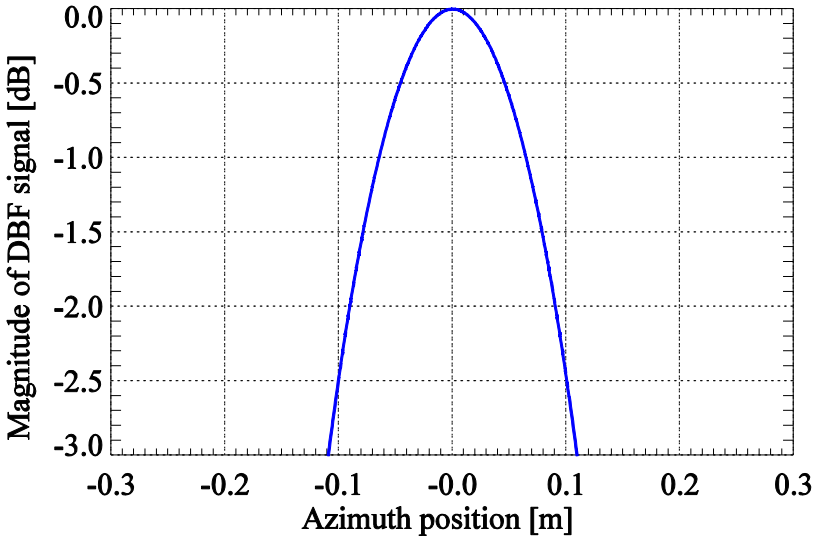

Figure 5.2 – Zoom of magnitude of focused point target signal reconstructed using LCMV DBF

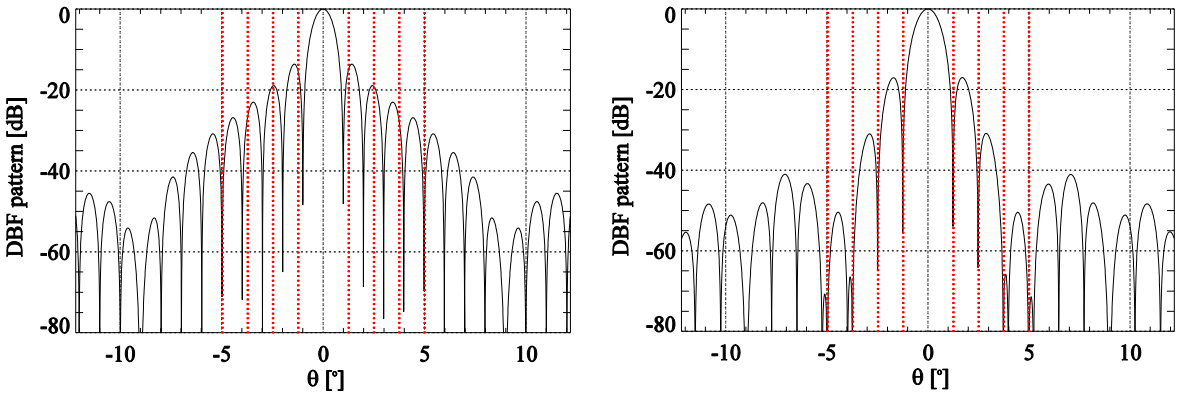

a) MVDR DBF b) LCMV DBF

Figure 5.3 –DBF patterns for center Doppler frequency

5.2 – DBF Using Estimated Patterns and Estimated Covariance Matrix

In this subsection, the complex patterns were estimated from low noise signals, with 10 dB SNR, since low noise is required for accurate pattern estimate, while the signals that were combined by DBF and from where the noise covariance matrices were estimated had -8 dB SNR, that is realistic since usually SAR raw signals have low SNR.

Fig. 5.4 and 5.5 show simulated examples of estimated noise covariance matrices in dB where the terms are normalized by the maximum value. In Fig. 5.4 the estimation was made from noise only measurements and in Fig. 5.5 the estimation was made directly from the signals. The matrix applied on the DBF process was the one of Fig. 5.5.

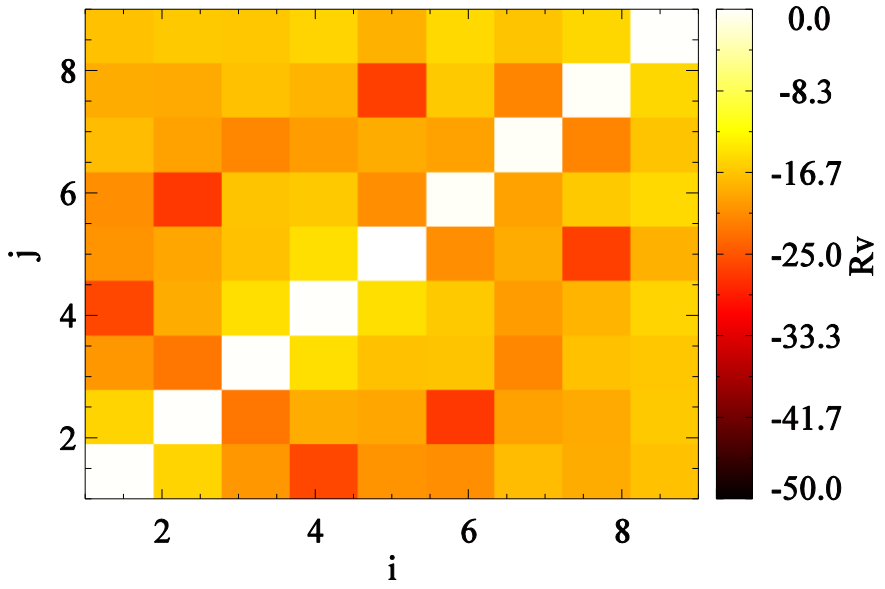

Figure 5.4 – Noise Covariance Matrix estimated from noise measurements

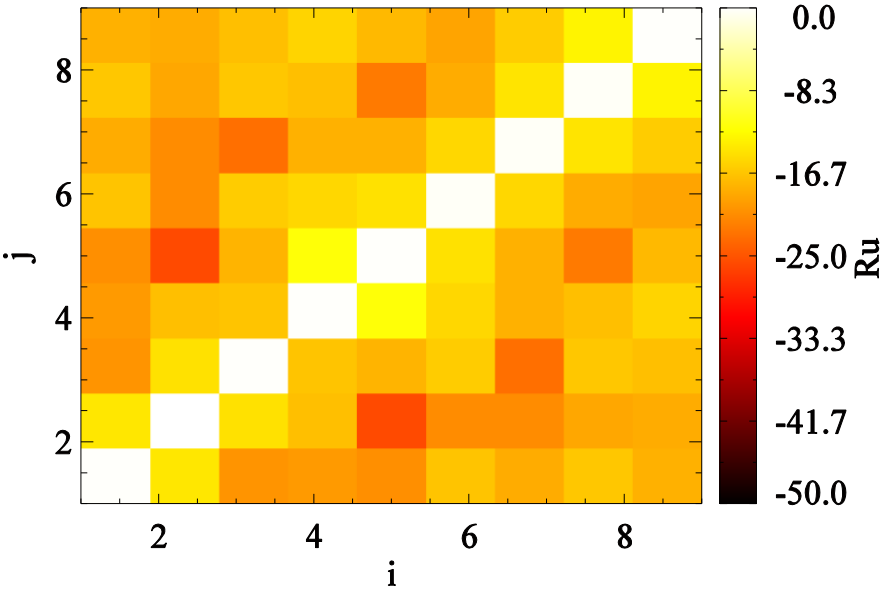

Figure 5.5 – Noise Covariance Matrix estimated from the signals

We can see that both estimated matrices are approximately diagonal, the diagonal elements are about 20 dB higher than the other elements.

Also we notice that the diagonal elements have the same value, what is expected because the channels have the same SNR. What is also possible to notice is that the matrices estimated by the two different methods are similar to each other.

In Fig. 5.6 the normalized compressed SAR signal of the point target for a single channel is shown. We can see the ambiguities and that they are modulated by the envelope of the two-

way pattern. When MVDR DBF is applied, shown on Fig. 5.7 a), we can see that the main signal is maximized and that there is an improvement of about 15 dB in terms of SNR. Finally, when the LCMV DBF is applied, shown on Fig. 5.7 b), the ambiguities are suppressed.

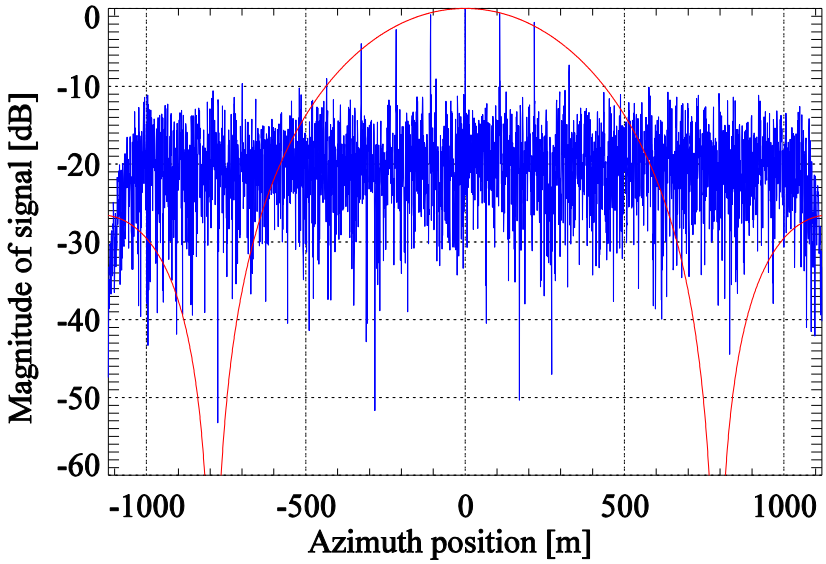

Figure 5.6 – Magnitude of focused noisy point target signal of a single Chanel

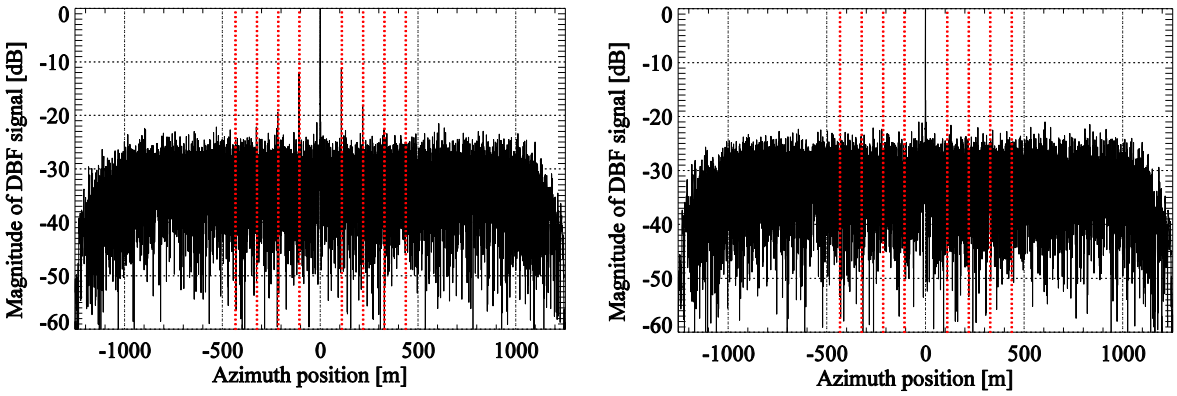

a) MVDR DBF

b) LCMV DBF

Figure 5.7 – Magnitude of focused noisy point target signal reconstructed using DBF

5.3 – DBF- Presence of Range History Estimate Errors and Noiseless Case

This section investigates the effect of Range history estimate errors on the construction of the Green's function (Equation 4.7) and consequently how those errors reflects on the

estimated patterns (Equation 4.3). Later, those estimated patterns are applied on DBF process to see the effect of those patterns errors on the suppression of ambiguities.

The first case considered is the one where the range error is azimuth dependent, as shown in Fig. 5.8. The range error is more or less random but smooth, simulating for example the vibration of the sensor and the maximum range error is equal to the wavelength ($\Delta R_{máx}(y, y_0) = \lambda$). Fig. 5.9 shows the simulated example of the comparison between the estimated and the analytical patterns for one channel, where the pattern in black is the estimated pattern and the pattern in red is the analytical pattern.

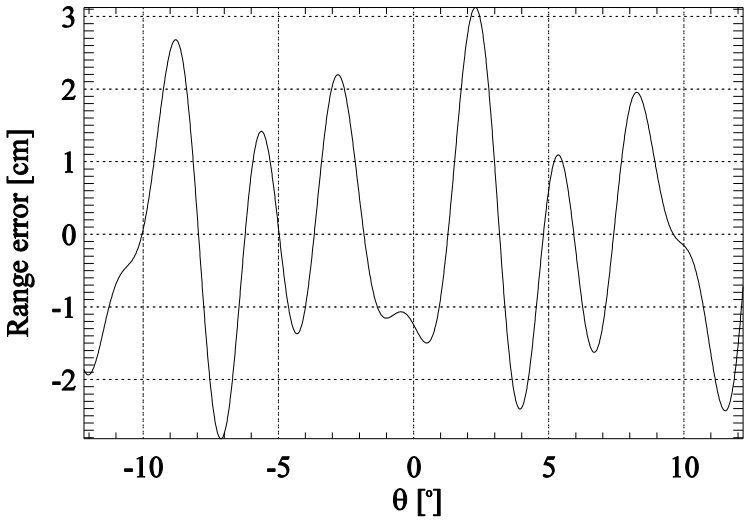

Figure 5.8 – Azimuth dependent range error

Fig. 5.9 a) shows that the estimation of the magnitude of the patterns was not affected by the range error, as expected from equation (4.7). Although, from Fig. 5.9 b) we notice that azimuth dependent range errors, even if small compared to the range history (in this case smaller than λ causes significant phase errors on the estimated patterns. This happens because, on the phase of the error phasor on equation (4.7), the range error $\Delta R(y, y_0)$ is normalized by λ, so a range error $\lambda/4$ is enough to cause a phase error of π rad.

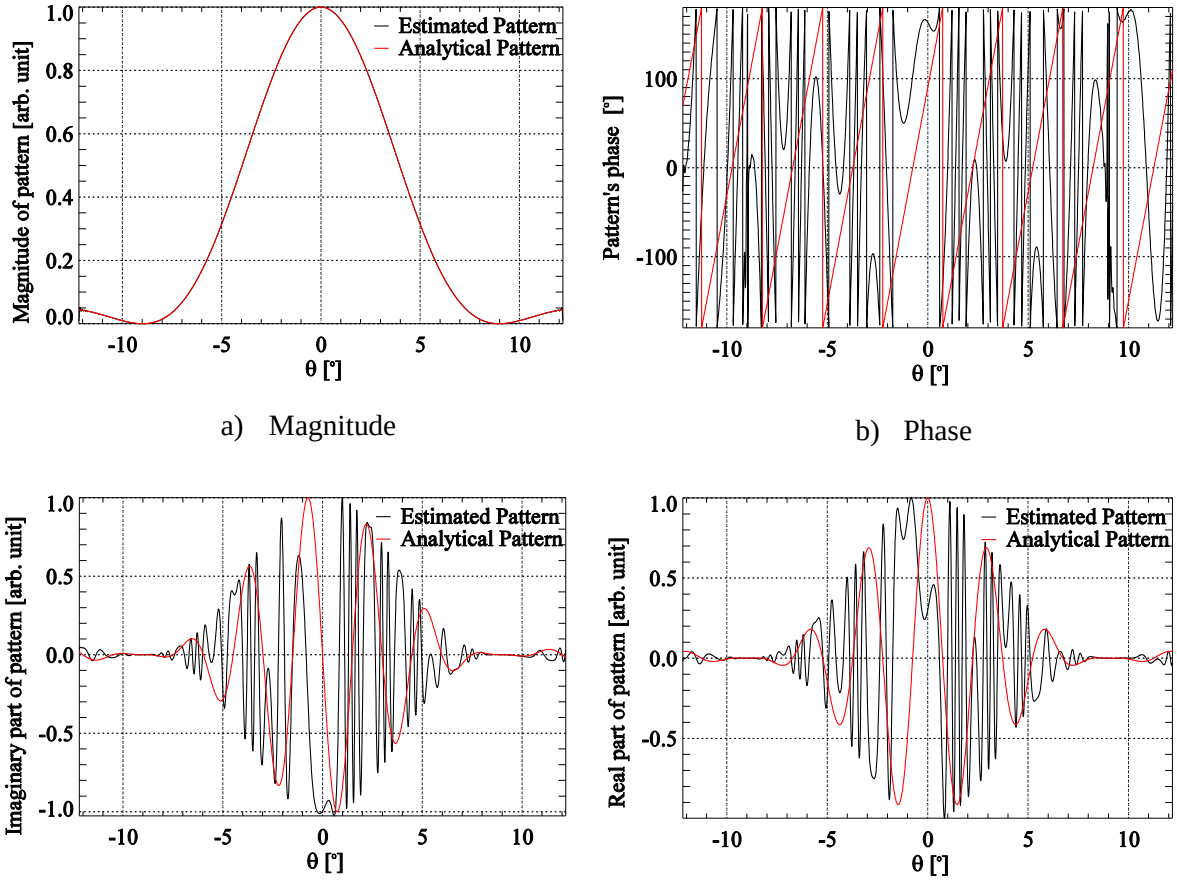

a) Magnitude

b) Phase

c) Imaginary part

d) Real part

Figure 5.9 – Comparison between Analytical and Estimated patterns with azimuth dependent errors

Fig. 5.10 a) shows when those patterns with phase errors are applied on MVDR DBF. The main signal is still maximized and we can see the ambiguities. But when LCMV DBF is applied (Fig. 5.10 b), we see that the ambiguities no longer are well suppressed, due to the phase errors on the estimated patterns.

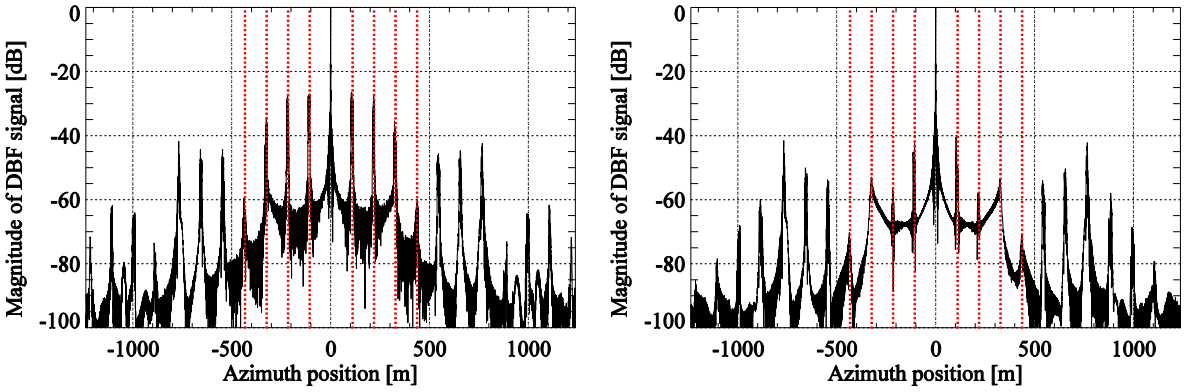

a) MVDR DBF b) LCMV DBF

Figure 5.10 – Magnitude of focused point target signal reconstructed using DBF applying patterns with azimuth dependent phase errors

Now, considering the range error constant in azimuth, where the estimated range history has a fixed range error equal to one sixth the wavelength ($\Delta R\,(y, y_0) = \lambda/6$), as shown in Fig. 5.11, we have from equation (4.7) that the error is a constant phasor multiplying the estimated patterns, so the patterns' magnitude estimate shouldn't be affected and the phase error is constant with azimuth, reflecting in just a phase shift on the patterns' phase estimate. Fig. 5.12 shows the simulated example of the comparison between the estimated and the analytical patterns for one channel, where the pattern in black is the estimated pattern and the pattern in red is the analytical pattern. As expected, Fig. 5.12 a) shows that the estimate of the magnitude of the patterns was not affected by the range error and Fig. 5.12 b) shows that the constant range error leads to a constant shift on the phase of the estimated patterns, in this case $2\pi/3$ rad. Since the error is a constant phasor multiplying the estimated patterns, and it is the same for all the channels, it shouldn't affect the DBF process. Indeed, when observing Fig.s 5.13 a) and 5.13 b), when those estimated patterns were applied on MVDR and LCMV DBF respectively, there are no differences from the error free case, depicted on Fig. 5.1.

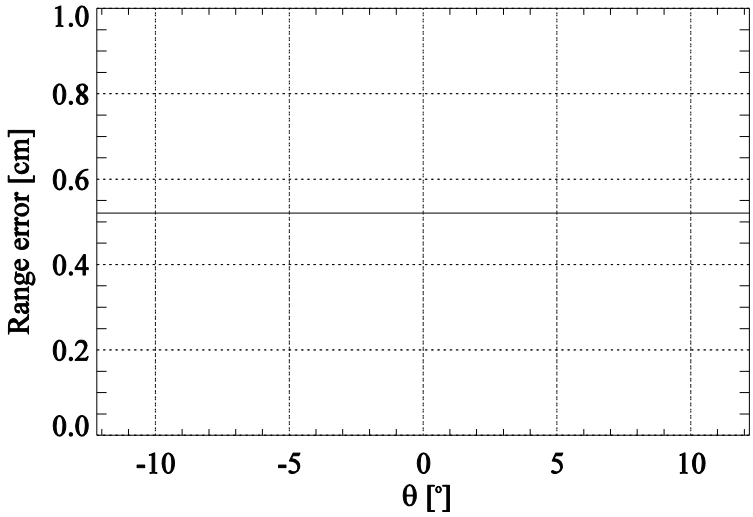

Figure 5.11 – Constant range error

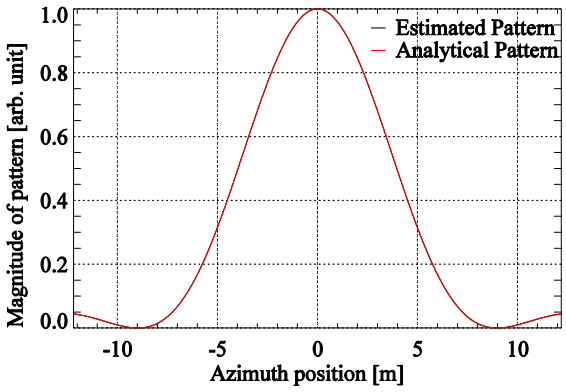

a) Magnitude

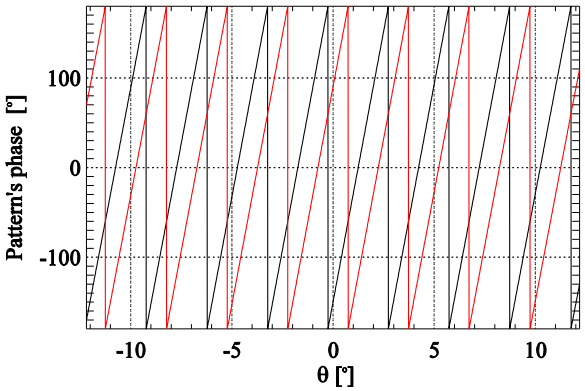

b) Phase

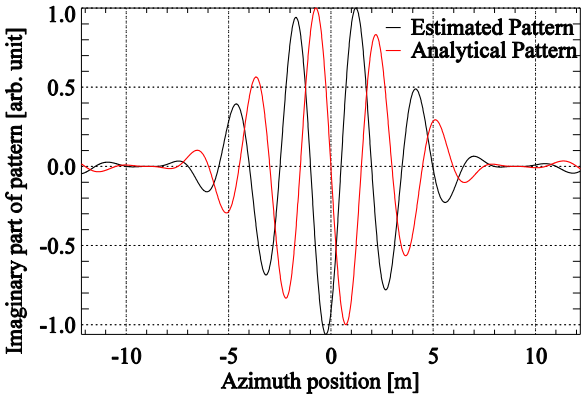

c) Imaginary part

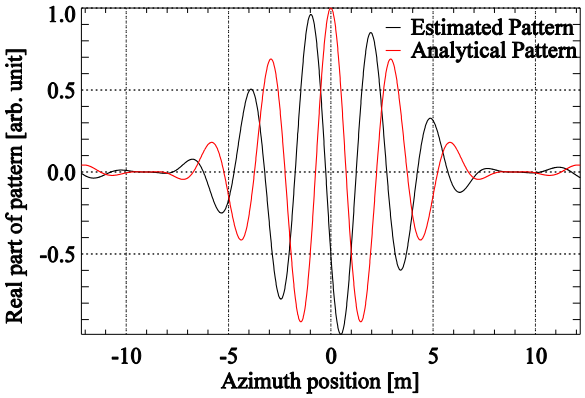

d) Real part

Figure 5.12 – Comparison between Analytical and Estimated patterns with constant phase error.

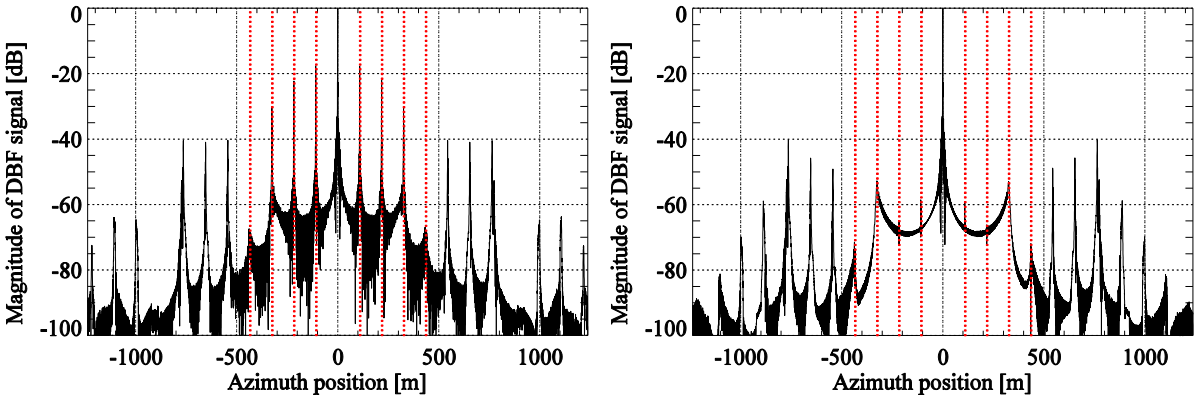

a) MVDR DBF b) LCMV DBF

Figure 5.10 – Magnitude of focused point target signal reconstructed using DBF applying patterns with constant phase errors

5.4 – Noise Influence on the DBF Process

The objective of this subsection is to analyze the effect that the noise level on the estimation of the patterns have on the suppression of ambiguities.

First, the signals that were combined by DBF to form the final signal had no noise, so that the effect of the noise on the estimated patterns were clearly shown. Fig. 5.11 a) to Fig. 5.11 d) shows when complex patterns estimated, from signals with SNR of 15 dB , 10dB, 5dB and 0 dB respectively were applied on LCMV DBF.

Those figures show the expected, that the performance degrades with the decrease of the SNR. But the acceptable level of SNR is particular of each application, because it depends on the subapertures length on the frequency domain, that is, on how much noise can be eliminated by the low pass filter on the estimation process and the performance also depends on the SNR of the signals being reconstructed.

On Figures 5.12 a) and 5.12 b) are depicted the cases where the signals being combined by DBF have 15 dB of SNR and the patterns applied were estimated from signals of 5 dB and 0 dB of SNR respectively. We can see that the patterns estimated from 5 dB SNR signals are when applied on DBF are effective on suppressing the ambiguities under the noise flor, but when the patterns are estimated from 0 dB signals, the ambiguities are not suppressed under the noise.

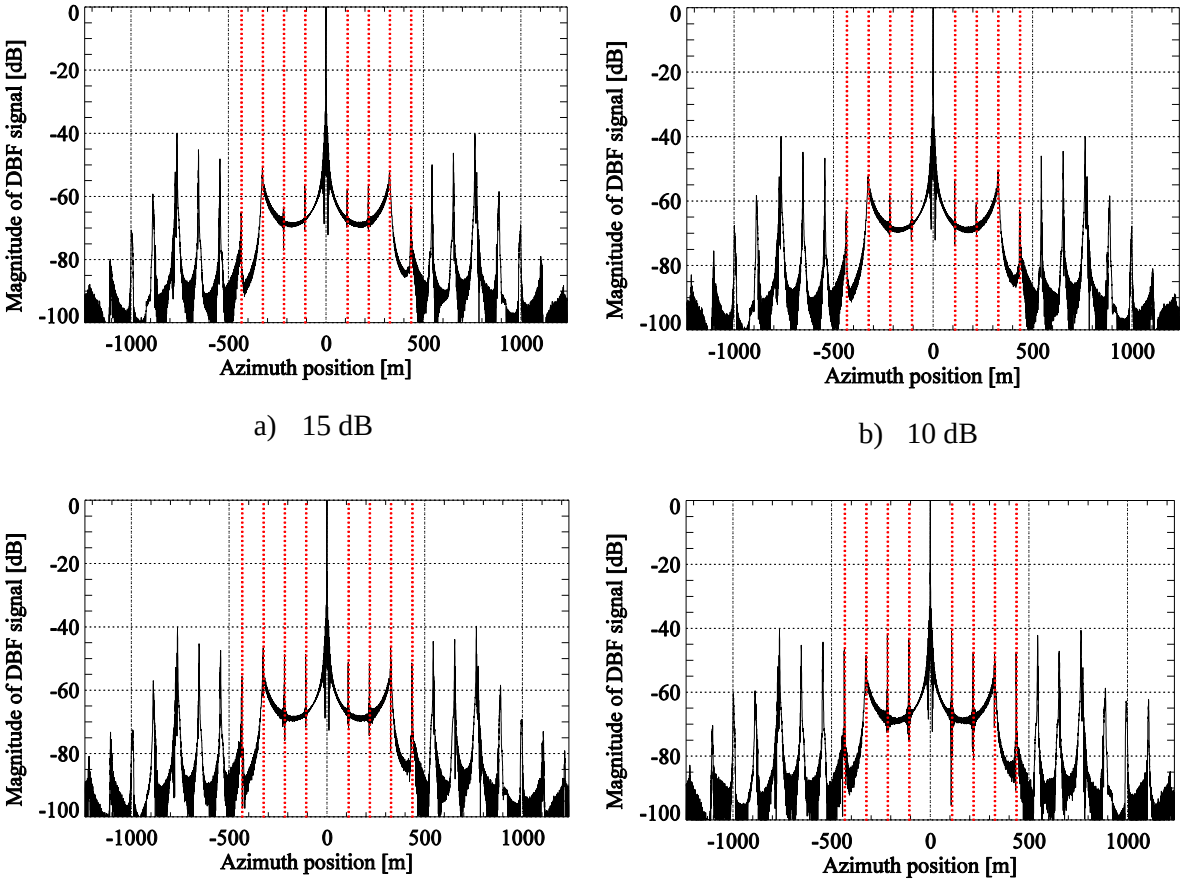

a) 15 dB

b) 10 dB

c) 5 dB

d) 0 dB

Figure 5.11 – Magnitude of focused point target signal reconstructed using DBF applying patterns estimated from noisy signals.

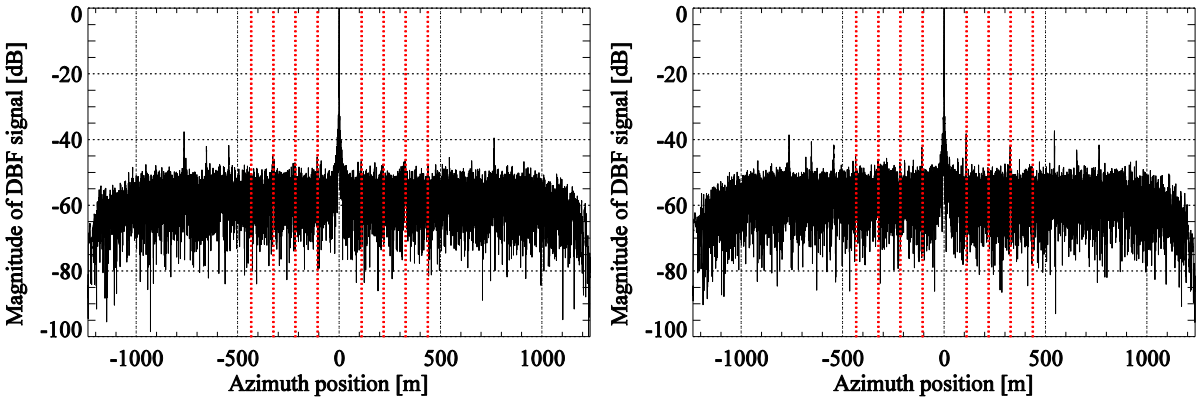

a) 5 dB

b) 0 dB

Figure 5.12 – Magnitude of focused point target signal reconstructed using LCMV DBF

6– Multichannel Demonstrator Experiments

In this section results from an experiment of a multichannel demonstrator with planar array are shown in order to explain how the complex patterns estimation works in practice.

6.1 – Experiment set up

The hardware of the experiment consisted of a reconfigurable radar system, depicted on Fig. 6.2, combined to a receiving planar array and a single transmitting element as depicted on Fig. 6.3. The support of the antenna system was attached to a wagon, travelling on a rail on velocity of 0.1 m/s and the target, a corner reflector, was placed on a sand field at an unknown distance from the rail, as depicted on Fig. 6.1.

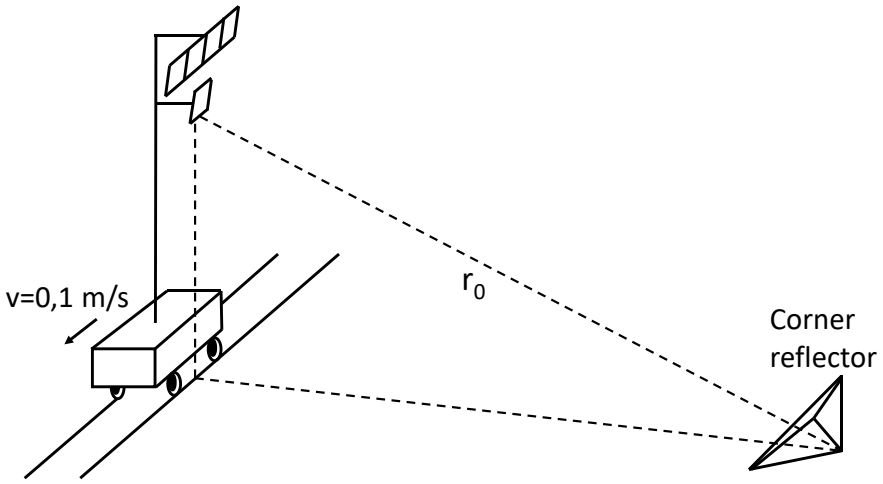

Figure 6.1 – Experiment set up

On the demonstrator, the chirp signal is generated using an arbitrary waveform generator (AWG) and converted to the X-band using a mixer and analog signal generator (PSG). Then the signal is filtered, amplified and transmitted. At the receiver side, the echoes are received, amplified by a low noise amplifier (LNA), down converted and individually digitized.

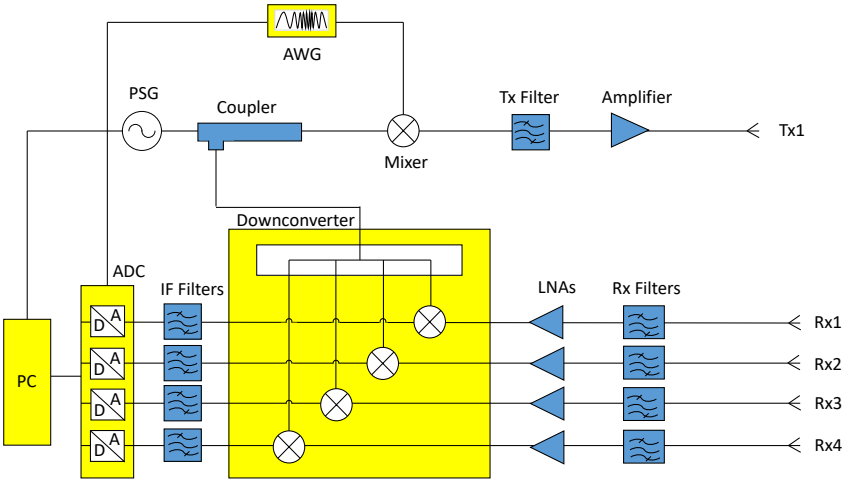

Figure 6.2 – Reconfigurable radar system

The receiving array was composed by four microstrip planar antennas on the azimuth direction, and a single transmitting element, with the same characteristics as the receiving elements (Fig. 6.3).

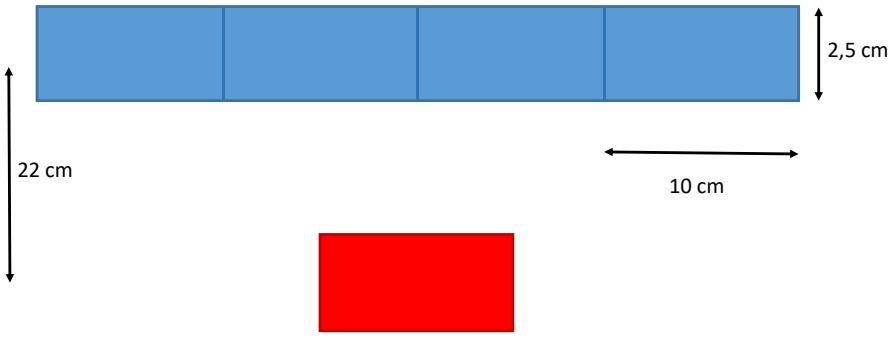

Figure 6.3 – Planar antennas system

6.2 – Range History Estimation

The first step necessary to estimate the complex patterns is to estimate the range history from the data for each channel. Fig. 6.4 shows the raw signal for the first channel. The next step is to range compress the signal, where the compressed signal is depicted in Figure 6.5. After that, for each azimuth position it is detected the range position of the highest power point, and those

points are placed in a Cartesian plane. At last, given that equation (2.13) can be approximated by a parabola, a parabola is fit on those points and the zero azimuth position is set corresponding to the position of minimum range distance, assumed to be the objects azimuth position. The final estimated range position for the first channel is depicted on Fig. 6.6.

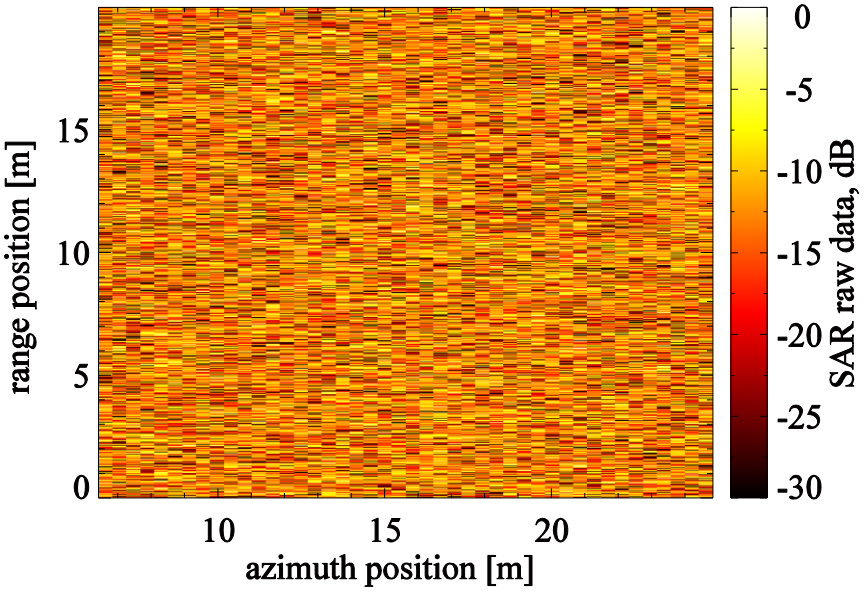

Figure 6.4 – SAR raw data

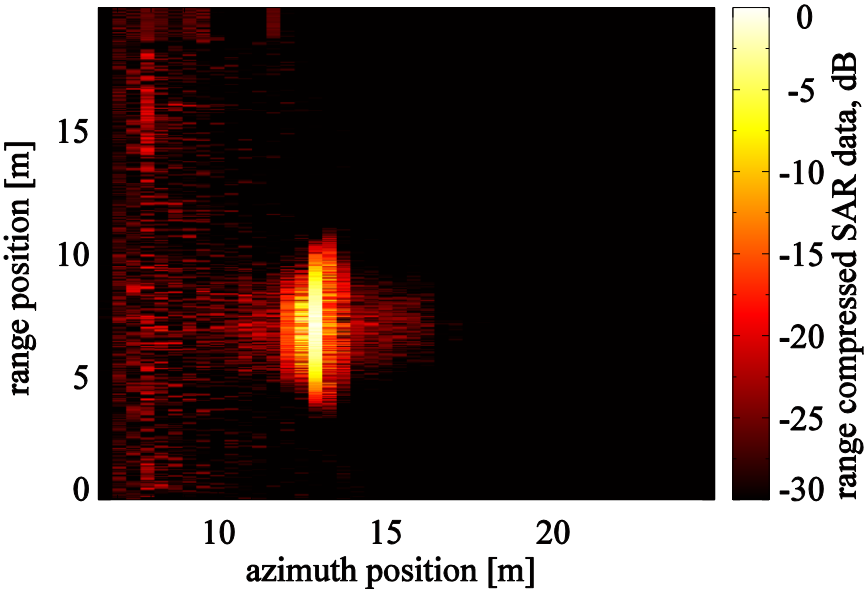

Figure 6.5 – Range Compressed SAR data

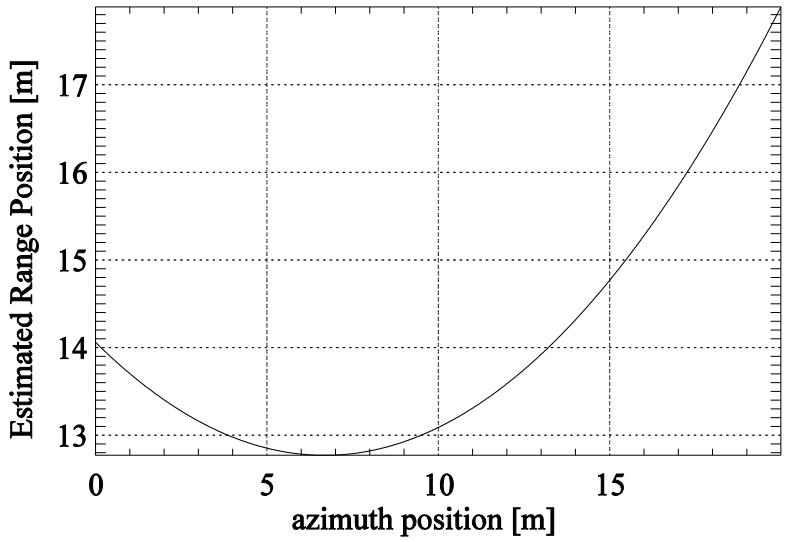

Figure 6.6 – Estimated Range Position

6.3 – Azimuth Signal Extraction

The next step is to extract the azimuth signal of each channel. For that, for each channel the raw data is range compressed, then it is done the RCM correction using the range history estimated on subsection 6.2 and at last it is selected the range line of the highest signal. Fig. 6.7 shows the signal of the first channel after RCM correction is done and Fig. 6.8 a) and 6.8 b) shows respectively the magnitude and real part of the azimuth signal of the first channel.

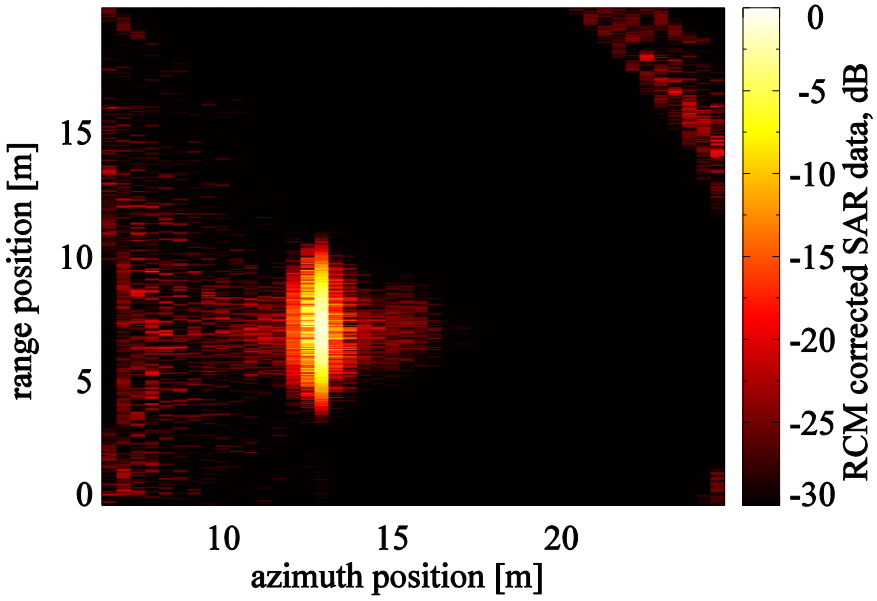

Figure 6.7 – RCM corrected SAR data

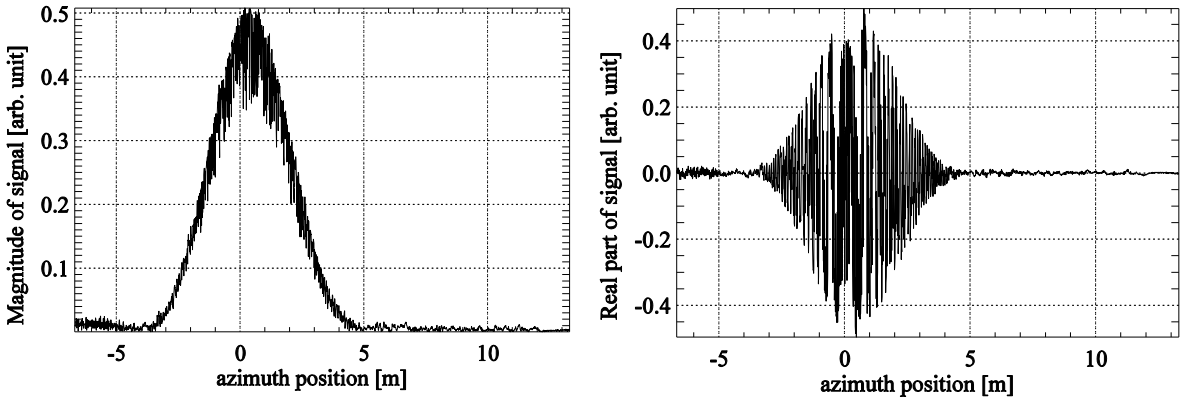

a) Magnitude b) Real part

Figure 6.8 – Azimuth signal

6.4 – Complex Pattern Estimation

6.4.1 – Elimination of Green's Function from The Signal

As explained previously on section 4, the first step to estimate the complex patterns is to reconstruct the Green's function and then eliminate it from the signal. For that, the range history estimated on subsection 6.2 is applied on equation (4.2), leading to the estimated Green's function $\hat{g}(y, y_o)$ and then the azimuth signals of each channel, extracted on section 6.3, are divided by the estimated Green's function, leading to noisy estimated patterns. Figs.6.19 a) and 6.9 b) shows respectively the absolute noisy pattern estimate for channel 1 and the real part of the noisy pattern estimate for the same channel.

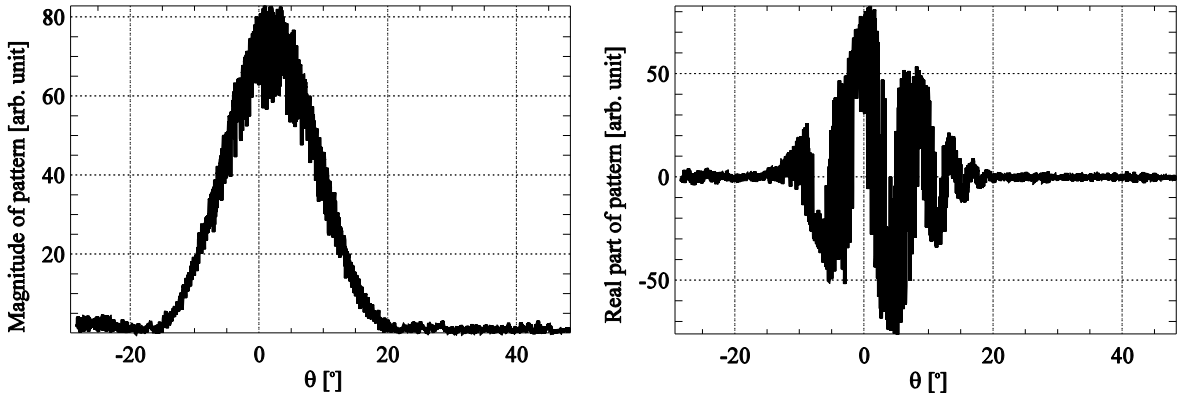

a) Magnitude b) Real part

Figure 6.9 – Noisy pattern

6.4.2 – Low Pass Filtering

Now the next step is to reduce the noise from the estimated patterns. For that, it is done the Fourier Transform of the noisy patterns and then it is applied a low pass filter. Fig. 6.10 shows the Fourier Transform of the noisy estimated pattern for the first channel and Fig. 6.11 shows the pattern after low pass filtering.

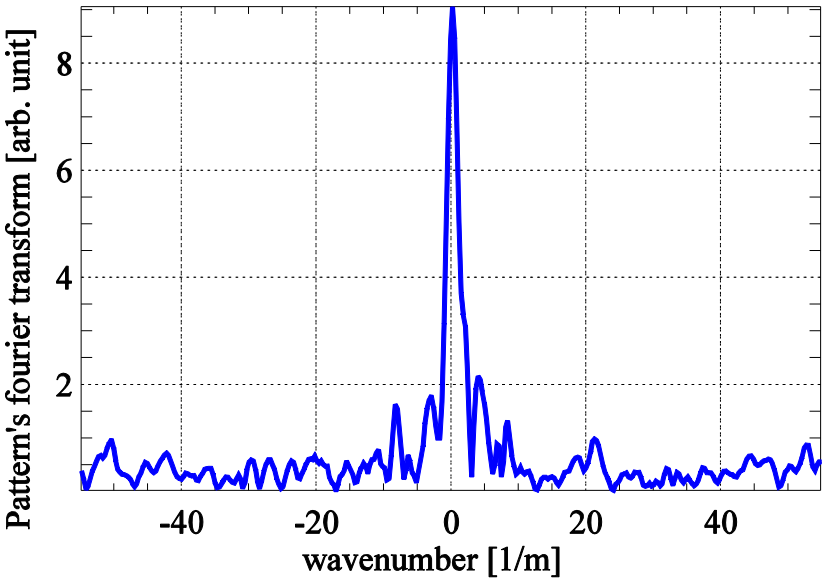

Figure 6.10 – Fourier Transform of the noisy estimated pattern

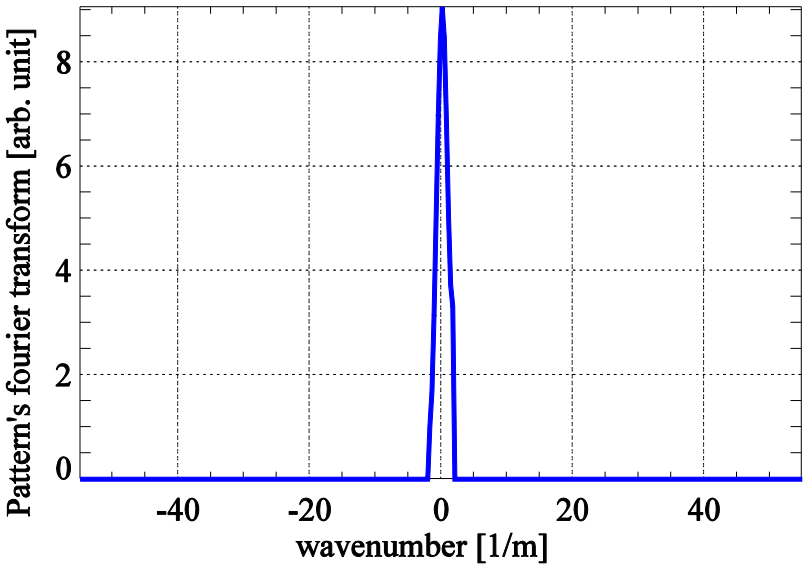

Figure 6.11 – Fourier Transform of the noisy estimated pattern after low pass filtering

6.4.3 – Inverse Fourier Transform

At last, to obtain the final estimate, it is done the Inverse Fourier Transform. Fig. 6.12 shows the absolute estimated (blue) and analytical (Orange) patterns superposing the magnitude of the estimated noisy patter only for the first channel, since the result of magnitude of the estimated patterns is very similar for all the channels, and Fig. 6.13 shows the real part of the estimated patterns of the four channels.

We can see differences between the estimated and analytical patterns due to experimental uncertainties such as: the sensor path was unknown, the wagons velocity was not really constant, the corner reflector is not a perfect point target, the azimuth position of the target was unknown and also the experiment was done in a windy day, causing the sensors vibration.

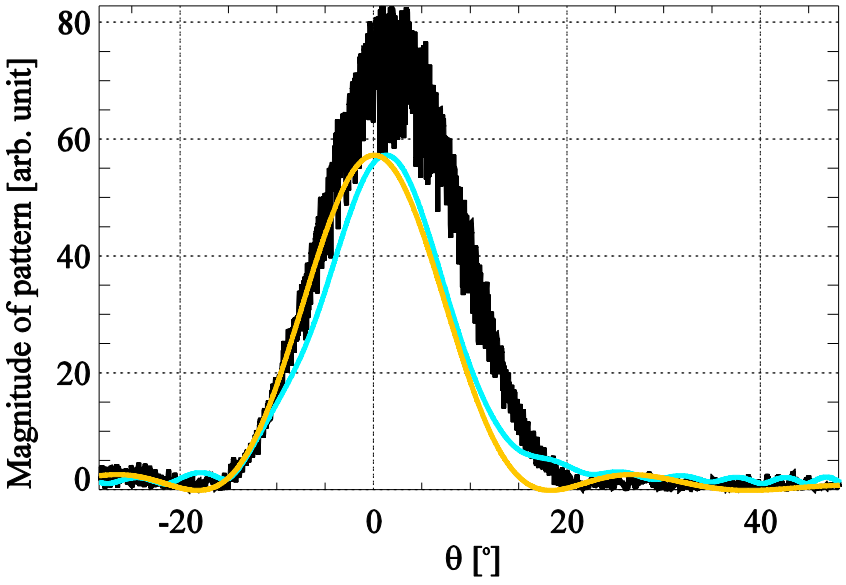

Figure 6.12 – Magnitude of patterns

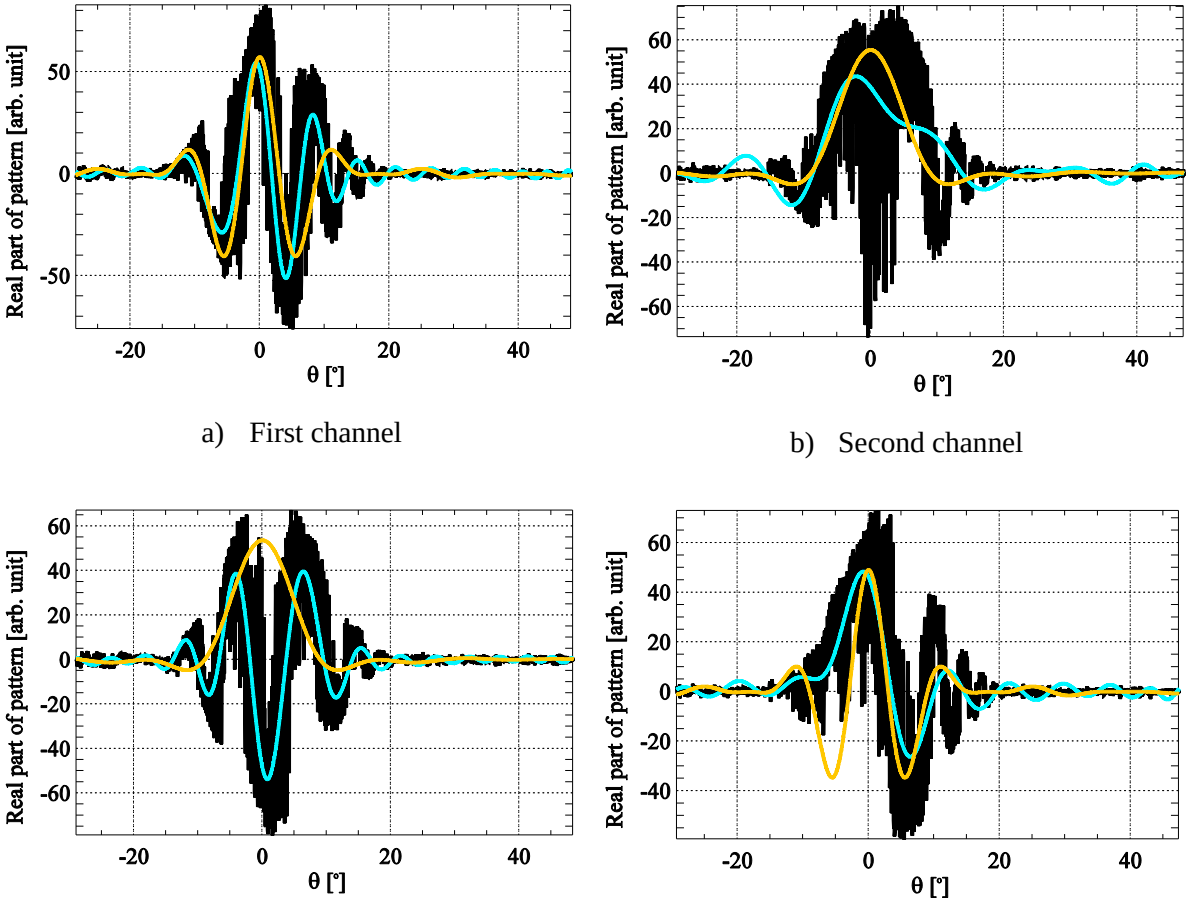

a) First channel

b) Second channel

c) Third channel

d) Fourth channel

Figure 6.13 – Comparison between noisy, analytical and estimated patterns

7 – Conclusion and Future Work

In order to provide a posteriori knowledge based beamforming method, that is, to enable DBF techniques to be effectively applied without prior information of the sensors antenna patterns and the channels noise covariance matrix, this thesis develops methods of estimating the complex azimuth antenna patterns from the data and also to estimate the channels noise covariance matrix from the data.

With respect to the estimate of the azimuth antenna patterns, the method based on a strong point target showed through simulations to be robust regarding the SNR variation, and since it is done in the time domain, it is possible to use undersampled data to estimate the patterns. On the other hand, it is very sensitive to errors on the range history estimate, that results in phase errors on the estimated patterns. Another complication of the method would be the requirement of a point target at each range position to estimate the complex patterns dependent of both θ and φ coordinates.

Next, the simulated patterns and noise covariance matrix were applied with DBF techniques to suppress ambiguities and optimize the image SNR. Then it was clear the effect that the phase errors from the estimated patterns had on the performance of DBF and suppression of ambiguities. Also, it was shown the depreciation of the DBF performance with the decrease of the SNR of the signals employed on the patterns estimation.

Finally, the method of estimating the complex array manifold from a point target SAR data was applied on practice, through a multi-channel demonstrator experiment using a corner reflector. Again, it is shown the methods high dependence of the targets range history.

The suggested future work is to conduct more robust experiment with Terra SAR-X (spaceborne radar) and a transponder, where the knowledge of the range history is more precise, in order to prove the methods effectiveness. Another suggestion is to investigate patterns estimation techniques based on distributes targets, where the estimate is done in Doppler domain from the signal covariance matrix, which properties are approached on [24].

References

[1] G. Krieger, I. Hajnsek, K. Papathanassiou, M. Eineder, M. Younis, F. D. Zan, S. Huber, P. Lopez-Dekker, P.Prats, M.Werner, Y. Shen, A. Freeman, P. Rosen, S. Hensley, B. Johnson, L. Villeux, B. Grafmüller, R. Werninghaus, R. Bamler, and A. Moreira, "Tandem-L: An Innovative Interferometric and Polarimetric SAR Mission to Monitor Earth System Dynamics with High Resolution,", in IEEE International Geoscience and Remote Sensing Symposium (IGARSS), Jul 2010, pp.253-256

[2] Curlander, J., and McDonough, R."Synthetic Aperture Radar–Systems and Signal Processing". New York: Wiley, 1991.

[3] Carrara, W., Goodman, R., and Majewski, R.*"Spotlight Synthetic Aperture Radar: Signal Processing Algorithm"*. Boston: Artech House, 1995.

[4] Tomiyasu, K. Conceptual performance of a satellite borne, wide swath synthetic aperture radar. *IEEE Transactions on Geoscience and Remote Sensing,GRS-19* ,1981, pp.108-116.

[5] Moore, R. K., Claassen, J. P., and Lin, Y. H. "Scanning spaceborne synthetic aperture radar with integrated radiometer".*IEEE Transactions on Aerospace and Electronic Systems*, AES-17 ,1981, pp.410-421.

[6] De Zan, F., and Monti Guarnieri, A. M. "TOPSAR: Terrain observation by progressive scans".*IEEE Transactions on Geoscience and Remote Sensing-44* , 2006, pp. 2352-2360.

[7] A. Currie and M. Brown, "Wide-swath SAR," *IEE Proceedings-F Radar and Signal Processing*, vol. 139, no.2, Apr 1992, pp. 122-135.

[8] M. Younis, C. Fischer, and W. Wiesbeck, "Digital Beamforming in SAR Systems," *IEEE Transactions on Geoscience and Remote Sensing*, vol. 41, no. 7, Jul 2003, pp.1735-1739.

[9] N. Gebert, G. Krieger, and A. Moreira, "Digital Beamforming for HRWS-SAR imaging: System Design, Performance and Optimization Strategies," in *IEEE Insternational Geoscience and Remote Sensing Symposium (IGARSS),* Aug 2006, pp. 1836-1839.

[10] G. Krieger, N. Gebert, M. Younis, F. Bordoi, A. Patyuchenko, and A. Moreira, "Advanced Concepts for Ultra-Wide-Swath SAR Imaging," in *European Conference on Synthetic Aperture Radar (EUSAR),* vol.2, Jun 2008, pp.31-34.

[11] Gerald Benitz, "Adaptive Beamforming for SAR Ambiguity Rejection", *MIT Lincoln Laboratory*, March 2004.

[12] M. Rangaswamy,F.C.Lin,K.R.Gerlach,"Robust adaptive signal processing methods for heterogeneous radar clutter scenarios", *Signal Process.84* ,Nov 2004,pp.1653–1665.

[13] Z.Yang,X.Li,H.Wang,W.Jiang,"Adaptive clutter suppression based on iterative adaptive approach for airborne radar",*Signal Process.93* , Dec 2013, pp.3567–3577.

[14] B.D.Wang and J.Bao, "Adaptively iterative weighting covariance matrix estimation for airborne radar clutter suppression", *Signal Processing 106,* 2015, pp.282–293

[15] O.Ledoit,M.Wolf,Awell,"Conditioned estimator for large dimensional covariance matrices",*J.Multivar.Anal.88,* Feb 2004, pp.365–411.

[16] Y.L.Chen,A.Wiesel,Y.C.Eldar,A.O.Hero,Shrinkage "Algorithms for MMSE covariance estimation" ,*IEEE Trans. Signal Process.58,* Oct 2010,pp.5016–5029.

[17] F.Gini,M.V.Greco,"Covariance matrix estimation for CFAR detection in correlated heavy tailed clutter",*SignalProcess.82,* Dec 2002, pp.1847–1859.

[18] J. L. Álvarez-Pérez, M. Schwerdt, M. Bachmann" TerraSAR-X Antenna Pattern Estimation by Complex Treatment of Rain Forest Measurements"; *Geoscience and Remote Sensing Symposium,* IGARSS 2006, Denver, USA, July 2006.

[19] Markus Bachmann,Marco Schwerdt, and Benjamin Bräutigam, "Accurate Antenna PatternModeling for Phased Array Antennas in SAR Applications-Demonstration on TerraSAR-X"**,***International Journal of Antennas and Propagation Volume 2009* , 2009, Article ID 492505, 9 pages.

[20] A. Monti Guarnieri, D. D'Aria., "Wide-Angle Azimuth Antenna Pattern Estimation in SAR Images, " *IEEE Xplore Conference: Geoscience and Remote Sensing Symposium, 2003. IGARSS '03. Proceedings. 2003 IEEE International,* Volume: 5.

[21] Cumming, I. G.; Wong, F. H. ,"Digital Processing of Synthetic Aperture Radar Data: Algorithms and Implementation. Boston": Artech House, 2005.

[22] W.L. Stuttzman, "Antenna Theory and Design". John Wiley & Sons, Inc. 1981

[23] S. Huber, M. Younis, A. Patyuchenko, G. Kriegermler, and A. Moreira," Spaceborne Reflector"SAR Systems with DigitalBeamforming",IEEE Transactions on Aerospace and Eletronic Systems ,Vol. 48, Oct 2012 , pp.3473-3493.

[24] Attia, E.h and,Steinberg"" Self-cohering Large Antenna Arrays Using the Spatial Correlation Properties of Radar Clutter",IEEE Transactions on Antennas and Propagation Vol. 37**,** January 1989, pp. 30-38.

FOLHA DE REGISTRO DO DOCUMENTO

1. CLASSIFICAÇÃO/TIPO	2. DATA	3. REGISTRO N°	4. N° DE PÁGINAS
TC	21 de novembro de 2016	DCTA/ITA/TC-032/2016	68

5. TÍTULO E SUBTÍTULO:

A posteriori knowledge based digital beamforming concepts demonstrated with multi-channel SAR-data.

6. AUTOR(ES):

Rayssa Freitas Carvalho

7. INSTITUIÇÃO(ÕES)/ÓRGÃO(S) INTERNO(S)/DIVISÃO(ÕES):

Instituto Tecnológico de Aeronáutica – ITA

8. PALAVRAS-CHAVE SUGERIDAS PELO AUTOR:

Beamforming digital, Ambuiguidades azimutais, Radar de Abertura Sintética.

9.PALAVRAS-CHAVE RESULTANTES DE INDEXAÇÃO:

Radar de abertura sintética; Largura da faixa; Processamento de imagens; Detecção de sinais; Telecomunicações; Engenharia eletrônica.

10. APRESENTAÇÃO: **X Nacional** **Internacional**

ITA, São José dos Campos. Curso de Graduação em Engenharia Eletrônica. Orientador: Prof.Dr. Alexis Tinoco Salazar; coorientador: Dr. Sigurd Huber. Publicado em 2016.

11. RESUMO:

Future SAR applications such as disaster monitoring or detection of biomass changes on a global scale demand large swath widths and high resolution at the same time. A high azimuth resolution raises the need of a high pulse repetition frequency (PRF) in order to sample the signal adequately and avoid azimuth ambiguities in the SAR imaging process. However, the high PRF limits the swath width. To overcome this limitation, a solution is to split the receiving antenna into multiple sub-apertures and then combine the sub-apertures signals using digital beamforming techniques to suppress the azimuth ambiguities. Since digital beamforming techniques require precise knowledge of the antenna patterns, a first investigation of this thesis deals with the estimation of the complex azimuth antenna patterns from point target data. These estimated patterns are then applied in an a posteriori beamforming process, meaning that no a priori information in terms of pattern knowledge is required. Here, basically two concepts are presented, the first being an SNR optimizer and the second dedicated to the suppression of azimuth ambiguities. In a second analysis the requirement of no a priori information is dropped insofar that only the so called noise channel covariance matrix is estimated from the data. The beamforming is performed on the basis of the array steering vector, assumed to be known a priori.

12. GRAU DE SIGILO:

(X) OSTENSIVO **( ) RESERVADO** **( ) SECRETO**